



## Research Article

# Preparation of Superhydrophobic Multiscale Films for Oil-Water Separation in a Harsh Environment

Depeng Li,<sup>1</sup> Jinyang Fan ,<sup>1,2</sup> Jie Chen ,<sup>1</sup> and Deyi Jiang<sup>1</sup>

<sup>1</sup>State Key Laboratory of the Coal Mine Disaster Dynamics and Controls, Chongqing University, Chongqing 400044, China

<sup>2</sup>Université de Côte d'Azur, CNRS, Observatoire de la Côte d'Azur, Géoazur, 250 Albert Einstein, 06560 Valbonne, France

Correspondence should be addressed to Jinyang Fan; [jinyang.f@cqu.edu.cn](mailto:jinyang.f@cqu.edu.cn)

Received 30 June 2019; Revised 2 September 2019; Accepted 12 September 2019; Published 5 November 2019

Academic Editor: Marián Palcut

Copyright © 2019 Depeng Li et al. This is an open access article distributed under the Creative Commons Attribution License, which permits unrestricted use, distribution, and reproduction in any medium, provided the original work is properly cited.

The problem of oil-water separation regarding oil-containing brine has been of much concern when using the oil pad water dissolution method to construct salt cavern reservoirs. In this paper, oil-water separation materials with micro-nano hierarchical structure were prepared on different metal substrates using chemical etching and electrophoretic deposition. And hydrophobic materials with a single micro/nano structure were also prepared; then, the surfaces were hydrophobized by various low surface energy modifiers. Thereafter, we analyzed and compared the surface morphology, chemical composition, and wettability of all the materials and found that brine contact angles on hierarchical structure surfaces were above 160° while the diesel was completely diffused. Furthermore, preparation parameters affecting the surface morphology and wettability of micro-nano composite structures were explored. Meanwhile, it was found that the surface of prepared composite structure could still maintain super-hydrophobic/lipophilic properties after exposure in air for 6 months, sliding 60 cm on sandpaper, or immersion in diesel/brine for 48 h. Moreover, the composite structure surface displayed improved corrosion resistance with corrected self-corrosion potential and lower corrosion current density. It was equally observed that the studied materials could be better adapted to the actual context of salt cavern reservoir construction and thus have great application prospects.

## 1. Introduction

In recent years, China has been undertaking large-scale constructions of salt cavern reservoirs [1], which have been widely used to store crude oil, natural gas, and other substances around the world [2, 3]. Most of those salt cavern underground reservoirs are constructed using the relatively advanced technology of oil pad water dissolution [4]. However, due to the difficulty in recovering the oil pad during the cavity construction period, a large amount of resources is wasted resulting in the increased cost of salt cavern construction. Meanwhile, improper treatment of the oily brine will cause great harm to the environment. With regards to that context, it seems urgent to conduct some research on the efficient separation and the recovery technology of oil in brine, and develop high-efficiency, low-energy separation materials. It is also imperative to protect the ecological environment, save energy, and favor the path of sustainable development.

At present, the methods that can be used for the separation of oil-containing brine are very limited, including gravity separation [5, 6], centrifugal separation [7, 8], air-float separation [9, 10], adsorption separation [11, 12], and membrane separation [13–15]. When conducting oil-water separation during the construction of salt caverns, the aforementioned methods present certain drawbacks such as the complexity of operations, the high cost of equipment, and the low separation efficiency [16, 17]. However, the adsorption method and the membrane separation method are relatively practical, thus supporting the fact that there is a certain application potential in the oil pad recovery process during salt caverns construction. While traditional adsorption or filtration materials have poor oil-water wettability, resulting in weak oil absorption and water resistance [18, 19]. Therefore, it is of great engineering and research significance to conduct a study on oil-water separation materials that can be used in a brine environment in order to get an excellent different wettability to oil and water.

The use of superhydrophobic materials for oil-water separation has been of high interest due to their high efficiency, low cost, and environmental benefits [20]. The superhydrophobic properties of the material surface mainly depend on the rough surface structure and the surface energy chemical composition [21, 22]. The most common rough structures are nanostructures and microstructures [23]. In some cases, a single nano [24] or microstructure [25] can also be superhydrophobic, but its practical use might be limited due to its poor strength and failing long-term stability performance. Several studies have found that some superhydrophobic substances in nature, such as lotus leaves [26], butterfly wings [27], and compound eyes of mosquitoes [28], have micro-nano hierarchical structures on their surface. Generally, it is preferable to introduce micro and nanoscale hierarchical structures into the substrates for ensuring superhydrophobicity after surface damage. Techniques such as chemical etching-anodic oxidation [29] and acid etching-boiling water immersion [30] are often used to create multiscale structures which are then hydrophobized by low surface energy modifier.

In this study, Al films were arranged on Al alloy and prepared along with stainless steel substrates using a combination of HCl/H<sub>2</sub>O<sub>2</sub> etching and electrophoretic deposition (EPD) [31]. The hydrophobicity and lipophilicity of the prepared materials were also carefully analyzed. Al alloy and stainless steel are very important engineering materials widely used in various industrial areas. Therefore, using them as substrates to prepare superhydrophobic materials will have broad application prospects. The hydrophobic surface with a single microstructure or nanostructure was also prepared to facilitate comparative research. In addition to the surface roughness, the surface chemical composition also has a decisive influence on the super-hydrophobic/lipophilic properties. We modified the surface of the prepared nanostructure with 1H,1H,2H,2H-perfluorodecyltriethoxysilane (FAS) and stearic acid (STA), respectively, to study the effects of different low surface energy modifiers on the super-hydrophobic/lipophilic properties of the material. The obtained results served to indicate that the FAS has extremely low surface energy to make the materials exhibit certain oleophobicity. The effects of the etchant composition, the etching time, the electric field strength during electrophoresis, and the electrophoresis time on the surface morphology and the wettability of the prepared surface were investigated. In addition, we also tested the wear resistance and corrosion resistance of the prepared samples through experimental tests. Furthermore, it was found that the sample surface maintains excellent super-hydrophobic/lipophilic properties after prolonged exposure to air and immersion in brine or diesel and exhibits superhydrophobicity for both acid and alkali droplets.

## 2. Experimental

**2.1. Preparation of Micro-Nano Hierarchical Structure Surfaces.** First, the Al alloy plates (type 5052), the stainless steel plates, and the screens (150 mesh) (type 201) (Southwest Aluminum Co. Ltd., Chongqing, China) were processed in advance and carefully polished by 2000#

metallographic sandpaper to remove the oxide layer on the surface. Then they were successively put into acetone, absolute ethanol, and deionized water (Kelong Reagent Co. Ltd., Chengdu, China) for ultrasonic cleaning for 10 minutes to remove surface dust, oil, and other impurities and then rinsed with pure water and blown dry with a hair dryer. For description convenience, samples obtained through this process were called P-Al (Polished Al) and P-SS (Polished stainless steel). Second, the treated Al alloy plate was disposed into a mixed solution made of 2 mol/L HCl and 2 mol/L H<sub>2</sub>O<sub>2</sub> (Kelong Reagent Co. Ltd., Chengdu, China) and allowed to react at a fixed room temperature for 3 minutes to obtain microstructured surface. For simplification purposes, the etched sample obtained by the process was called M-Al (Microstructured Al). Third, a nano-scale roughness structure was placed on the micro-structured substrate, and 0.1 g of the nano-Al powder (80 nm, Aladdin Industrial Inc., Shanghai, China) was diluted into 100 mL of a mixed solution of acetyl acetone and ethanol (vol. = 1 : 1) (Kelong Reagent Co. Ltd., Chengdu, China). After sealing with a plastic film, the whole mixture was subject to ultrasonic oscillation for 20 minutes, and a stable suspension for electrophoretic deposition was obtained. The micron-sized Al alloy substrate processed by etching was then used as a cathode and was immersed in the solution while vertically inserting the titanium plate (Southwest Aluminum Co. Ltd., Chongqing, China) working as an anode into the prepared suspension. The two electrodes were parallel to each other and had a fixed pitch of 1 cm. The electric field strength selected in the test was 10 V/mm, and the deposition time was 3 minutes. After the deposition was over, the cathode material was taken out from the suspension, carefully rinsed with absolute ethanol, and placed in a dry box for drying. The mass change value of the cathode material before and after electrophoresis was measured by an electronic balance. The rough sample prepared at this stage was an etch-deposited sample, and an MN-Al sample (Micro/nano-structured Al) was obtained. At this stage, using the same parameters as the above electrophoretic deposition, we prepared the nanostructured surface on the polished Al alloy substrate, which is referred to as N-Al (nanostructured Al). Finally, the rough surface was modified using low surface energy materials.

The preparation of superhydrophobic stainless steel materials is similar to that of Al alloy materials, but some parameters are slightly different. During the preparation, the pretreated dried stainless steel substrate was immersed in a mixed solution of 1.2 mol/L HCl and 1.5 mol/L H<sub>2</sub>O<sub>2</sub> for 5 minutes while the cathode was replaced with an etched stainless steel substrate during electrophoresis. However, other parameters were the same as the Al alloy. In the same time, nanostructured surfaces were prepared on polished stainless steel plates and screens. The prepared plate samples with different surface structures were marked as M-SS, N-SS, and MN-SS.

**2.2. Characterization.** We used a field emission scanning electron microscope (FESEM, JSM-7800F, Japan) to

characterize the surface morphology and microstructure of the prepared samples. The three-dimensional structure, contour morphology, and roughness of the sample surface were characterized by atomic force microscopy (AFM, MPF-3D-BIO, USA), white light interferometry (Zygo, Newview 7100, USA), and powder X-ray diffraction (XRD, ZD-3AX, Japan). The bond between the low surface energy modifiers and the surface of the sample was analyzed with the Fourier transform infrared spectrophotometer (FTIR, Nicolet iN10, USA). The contact angle optical tester (OCA20, German) was used to measure the static contact angle and sliding angle of the droplet on the surface of the sample, and the contact between the droplet and the surface of the sample was observed using a high-speed camera (Phantom V7.3, USA).

### 3. Results and Discussion

**3.1. Surface Morphology and Chemical Composition Analysis.** We examined the morphology of micron and micro/nano sample surfaces by FESEM. Figure 1(a) shows FESEM images of different magnifications of Al alloy substrates after etching in  $\text{HCl}/\text{H}_2\text{O}_2$  for 3 minutes. It can be seen that the surface after chemical etching becomes rough and uneven, and a large number of micro-sized discontinuous pits and rectangular boss structures are formed on the surface. It can also be observed from the high magnification diagram that these stepped structures are composed of approximately square brick structures with dimensions on the order of micrometers. Through further observation, we found that the surfaces of these stepped structures themselves are relatively flat. Figure 1(b) shows the surface topography of the samples prepared by etch-electrophoresis. From the macroscopic image, it can be seen that after the EPD, there are still microstructured units connected to each other on the surface of the sample, forming a rough and uneven structure (Figure 1 (b-1)). However, by magnifying the image further, it can be found that the surface of the stepped structure after EPD is not flat and covers numerous nanosized fine sand-like structures composed of tiny nanoscale particles which are connected to each other, forming a more tiny hole structure. In addition, it can be seen from the inset in Figure 1 (b-3) that these deposited nanostructures are similar in structure to the N-Al surface prepared by EPD, indicating that the nanoscale structure was successfully introduced by the EPD process without changing the micron-scale layered structure of the etched sample. Therefore, by combining etching and EPD processes, a binary composite rough morphology was successfully prepared on Al alloy substrate.

Figures 1(c) and 1(d) show FESEM images of different magnifications of the stainless steel substrates after different processes. Similarly to the Al alloy sample, after the stainless steel substrate is processed by etching, a large number of micron-sized pit structures and irregularly shaped pleats are formed on the surface of the sample, indicating that micron structure can be introduced into the stainless steel surface by the etching process. After the EPD process, the micron-scale structure on the surface of the sample is still visible and

compared with the rough surface of the stainless steel obtained by etching only, there is a uniform nanoscale deposition structure on the microscale pits and ridge structures after deposition. It is also possible to combine the above etching and EPD processes to obtain a binary rough morphology on stainless steel substrates.

To further compare the morphological differences between microstructures and micronanostructures, we observed the surfaces of Al alloy and stainless steel prepared by different processes using white light interferometer and atomic force microscopy. Figure 2 displays large-size white light interferograms of M-Al, MN-Al, M-SS, MN-SS, N-SS, and corresponding small-size atomic force microscopy images, respectively. Comparative observations show that under the  $\text{HCl}/\text{H}_2\text{O}_2$  etching system, microstep structures and concave fold structures are prepared on the surface of Al alloy and stainless steel, respectively. At the same time, it can be clearly seen from the morphology before and after the deposition process that the EPD process successfully creates nanoscale roughness on the surface of the etched microscale structure. The surface roughness of M-Al and M-SS by the atomic force microscopy test were  $R_a(\text{M-Al}) = 0.43 \mu\text{m}$ ,  $R_a(\text{M-SS}) = 0.17 \mu\text{m}$ , while the roughness of the surface of the etch-deposited samples was  $R_a(\text{MN-Al}) = 0.37 \mu\text{m}$ ,  $R_a(\text{MN-SS}) = 0.315 \mu\text{m}$ . After the EPD, the surface roughness of the Al alloy had decreased, but based on the wettability test and the superhydrophobic property, the MN-Al surface was superior to the M-Al surface. This indicates that the size of the surface roughness should not be too flat or too rough [32, 33]. If the surface roughness is too small, it will not allow the storage of the air cushion, while if it is too high, the droplets would have a large resistance when rolling on the surface, resulting in a large contact angle hysteresis. The surface of the stainless steel sample has become extremely rough from the relatively smooth surface before EPD.

The chemical composition of the samples in different preparation processes was tested by powder X-ray diffraction. Figure 3(a) presents the diffraction pattern of the blank sample, the microstructure sample, and the micro-nanostructure sample. For the Al alloy substrate, the diffraction peak positions of the samples before and after etching are compared, and they are found to be consistent with the standard diffraction peak of Al in JCPDS Standard Card No. 04-0787. It is shown that the composition of the micron-sized pit and the bump structure of the etched M-Al sample is Al. At the same time, the position of the diffraction peak of the MN-Al sample does not change after the EPD, which further confirms that the nanostructure observed in the FESEM is deposited Al particles. For the stainless steel substrate, results are shown in Figure 3(c). The powder X-ray diffraction patterns of the stainless steel samples before and after etching show obvious diffraction peaks around  $43.69^\circ$ ,  $50.98^\circ$ , and  $74.68^\circ$ , which is mainly the FeNi diffraction peak of the stainless steel substrate itself (JCPDS Card No. 03-1209), indicating that the composition of the stainless steel substrate remains unchanged after chemical etching. However, besides the diffraction peaks of the stainless steel substrate itself, five new characteristic diffraction peaks are observed near the diffraction angles of  $38.47^\circ$ ,  $44.74^\circ$ ,  $65.13^\circ$ ,



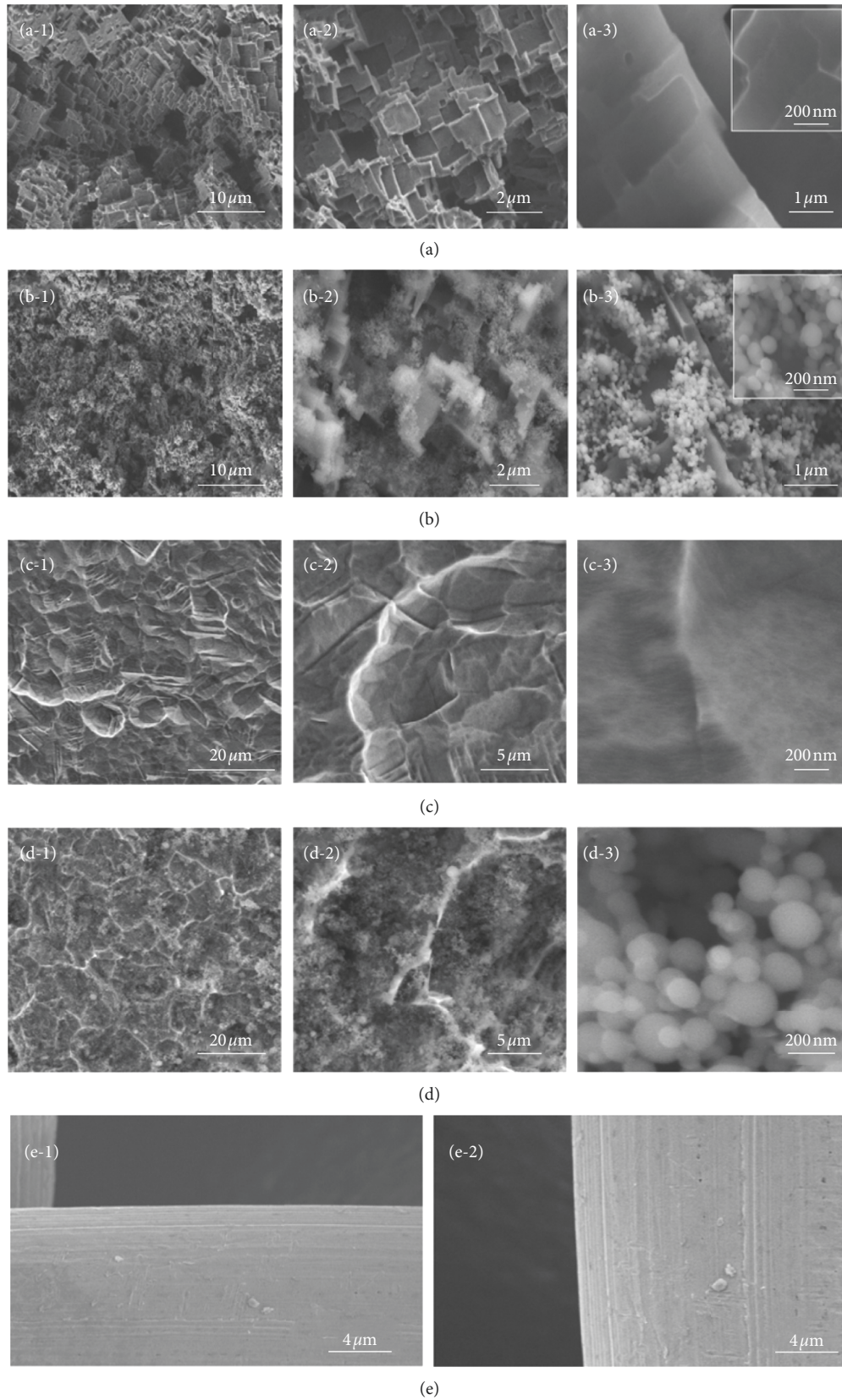


FIGURE 1: Low and high FESEM images of the (a) Al alloy and (c) stainless steel after etching process, (b) Al alloy and (d) stainless steel after the combination of etching and EPD treatments, (e) polished Al alloy surface.

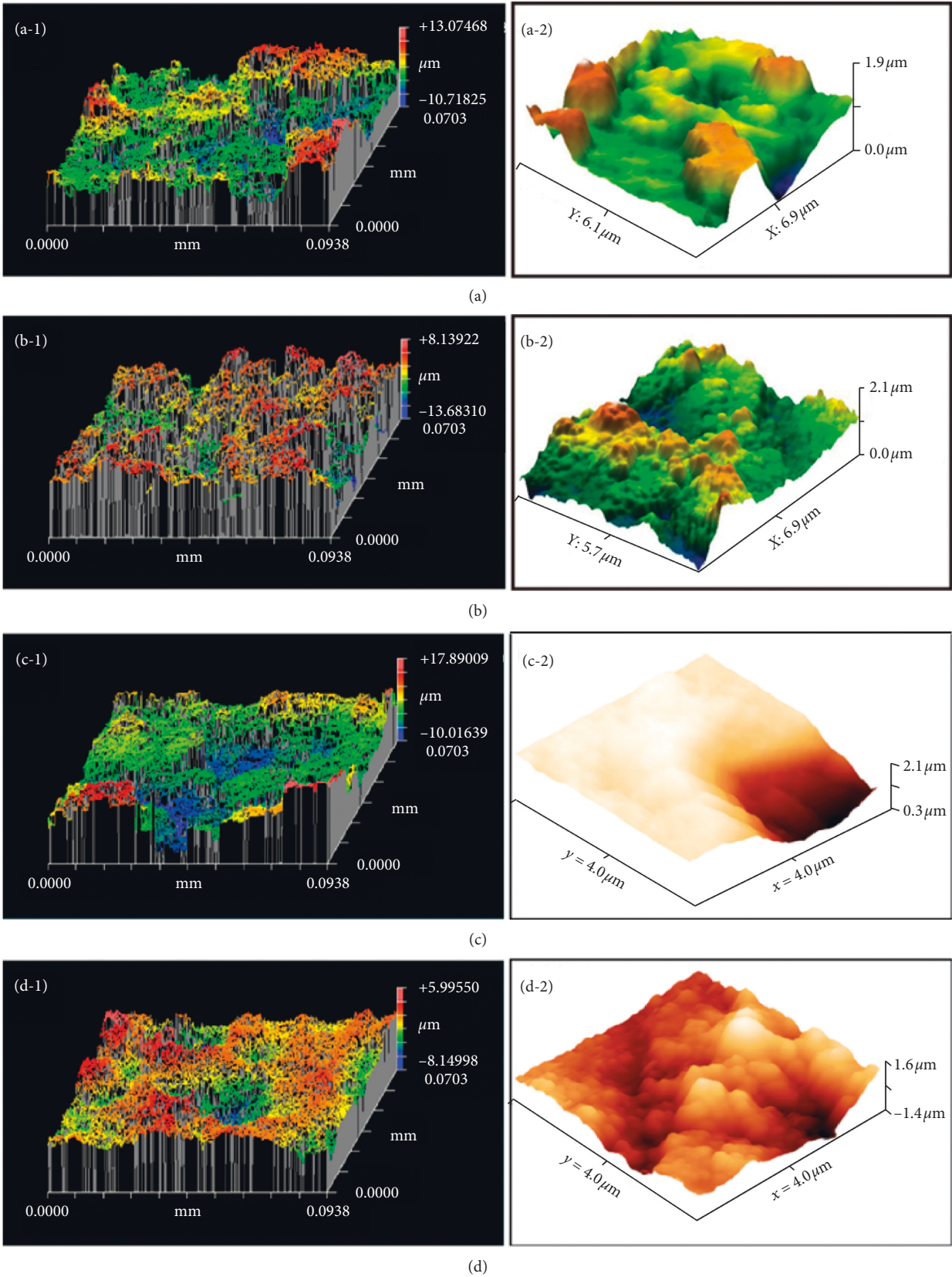


FIGURE 2: Continued.

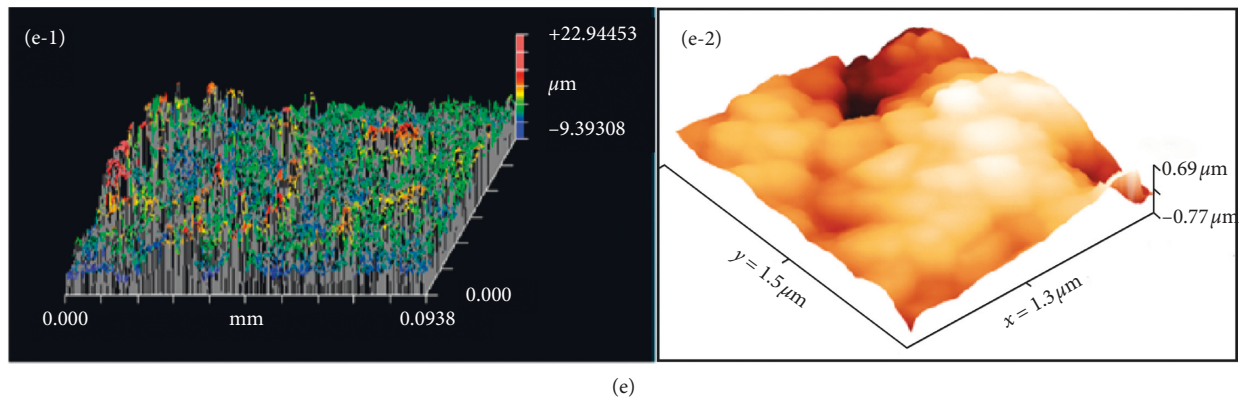


FIGURE 2: The 3D topography of (a) M-Al, (b) MN-Al, (c) M-SS, (d) MN-SS, and (e) N-SS surface.

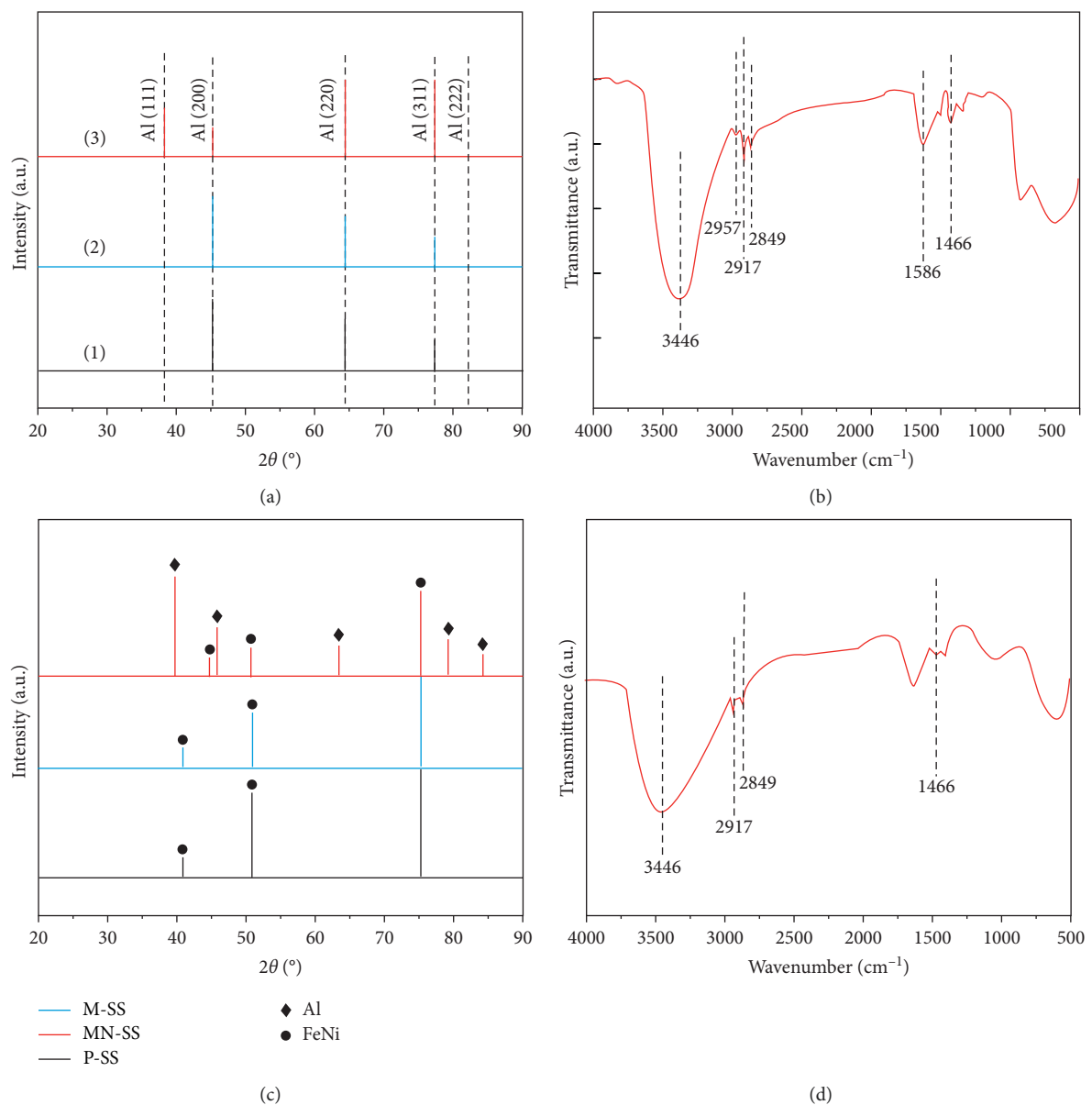


FIGURE 3: (a) The powder X-ray diffraction patterns of (1) P-Al, (2) M-Al, (3) MN-Al surface and (c) P-SS, M-SS, MN-SS surface, FTIR spectra of the (b) MN-Al and (d) MN-SS surface after STA modification.



78.23°, and 82.46° after the EPD. Each diffraction peak is identical to the JSPDS Standard Card No. 04-0787 of aluminum element, which represents the (111), (200), (220), (311), and (222) crystal faces of aluminum element, respectively. Through powder X-ray diffraction analysis, it is reasonable to infer that a film composed of nano-Al powder is introduced on the surface of the etched stainless steel by EPD.

The surface composition of the micro-nanostructures modified by STA was tested via FTIR. For the Al alloy substrate, results are shown in Figure 3(b). After modification by STA, the sample exhibited stretching vibration peaks of -CH<sub>3</sub> and -CH<sub>2</sub>- near 2957, 2849 and 2917 cm<sup>-1</sup>, which indicated that the surface of the sample contains a large number of hydrophobic groups of -CH<sub>2</sub>- and -CH<sub>3</sub>. Furthermore, the C=O stretching vibration peak corresponding to STA at 1703 cm<sup>-1</sup> disappeared, and a new OCO symmetric stretching vibration peak appeared at 1466 cm<sup>-1</sup>. Results for the stainless steel substrate are shown in Figure 3(d). Strong absorption peaks are detected at 3446, 2849, 2917, and 1466 cm<sup>-1</sup>, corresponding to vibration peaks of -OH, -CH<sub>2</sub>-, -OCO-, respectively. At the same time, the C=O free stretching vibration peak of the STA at 1703 cm<sup>-1</sup> disappeared, indicating that the STA successfully self-assembled on the surface of the sample. Therefore, the modified sample surface contains -CH<sub>2</sub>- hydrophobic groups, and these outwardly extending hydrophobic groups can effectively reduce the surface free energy [34].

**3.2. Wettability of Brine and Diesel Analysis.** In order to better explore the influence of surface structure change on surface wettability, this section systematically studied the surface wettability of materials obtained at different stages of the preparation process while maintaining the consistency of STA modification process. We conducted a comparative study on Al alloy and stainless steel materials with different surface morphologies, namely, P-Al, M-Al, N-Al, MN-Al and P-SS, M-SS, N-SS, MN-SS. We first tested the contact angle and sliding angle of brine and diesel droplets on the surface of four Al alloy materials. The results are shown in Figures 4(a) and 4(b). Figure 4(e) shows the contact angle image of brine on four different structural surfaces. For P-Al, the surface modified by STA changes from hydrophilic to hydrophobic, which is caused by the intrinsic hydrophobicity of the hydrophobic groups -CH<sub>3</sub> and -CH<sub>2</sub>- in STA long chain molecules. For the M-Al surface prepared by etching, the contact angle of the brine for the blank sample is increased from 106 ± 1.5° to 157 ± 2.8°, the sliding angle is reduced to 6 ± 2.7°, and the contact angle of the diesel is reduced from 29° to 9°. This indicates that the etched and modified samples have improved hydrophobicity and lipophilicity. However, we further found that the surface of MN-Al with micro-nano hierarchical structure has a higher super-hydrophobic/lipophilic ability with a brine contact angle of up to 167 ± 2.1° and a sliding angle of about 1° and that the diesel oil is completely diffused and the contact angle is 0°.

The enhancement of the wettability of different structural surfaces is explained by the Cassie-Baxter equation and

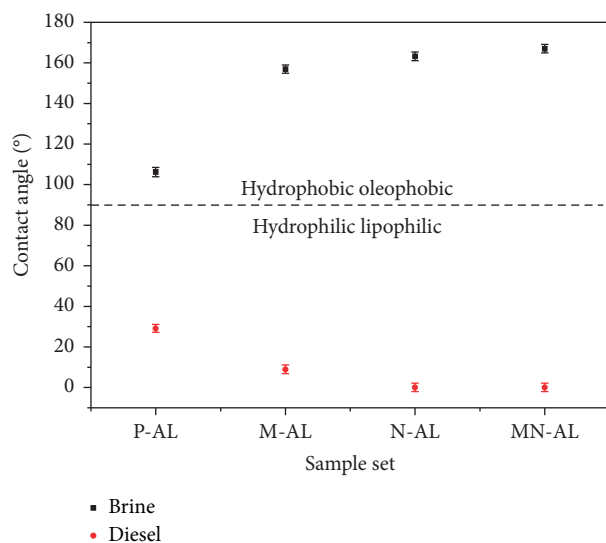
the Wenzel equation [35–37]. When the brine droplets are placed on the surface of the modified M-Al and MN-Al, they form a solid-liquid-gas three-phase contact interface with both surfaces. Substituting the respective contact angle values into the corresponding formula, we have

$$\begin{aligned}\cos 157^\circ &= f_{sv-m} (\cos 106^\circ + 1) - 1, \\ \cos 167.1^\circ &= f_{sv-mn} (\cos 106^\circ + 1) - 1.\end{aligned}\quad (1)$$

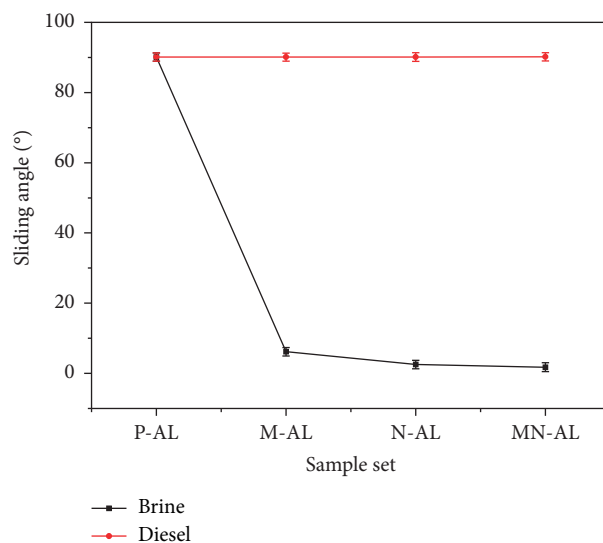
For the M-Al surface, the contact fraction of the solid-liquid interface is  $f_{sv-m} = 0.1097$ , and the area fraction of air is about 89.03%. For the MN-Al surface,  $f_{sv-mn} = 0.0354$ , and correspondingly, the area fraction of air is about 96.46%. It is higher than the area fraction of air on the M-Al surface, indicating that the micro-nano hierarchical configuration greatly increases the trapped air membrane area at the solid-liquid interface. The smaller contact area between solid and liquid also contributes to reducing the adhesion of the MN-Al surface to the brine droplets [38]. Furthermore, the true solid-liquid contact fraction of MN-Al is smaller than that of N-Al surface, indicating that the nano-film structure with multiscale structure is more conducive to reducing the solid-liquid contact area and solid-liquid adhesion, so there is a smaller contact angle hysteresis and the brine droplets tend to stay in a stable Cassie state. In addition, the air fraction on the surface of MN-Al is higher than that of N-Al (94.3%). These calculations further confirm that the coarse hierarchical structure and sufficient air content are key factors in achieving superhydrophobic performance [39]. It can be seen that a suitable micro-nano hierarchical structure is more favorable for superhydrophobicization of the surface than a single microscale structure or nanostructure.

We have also conducted a similar study on stainless steel materials. The wettability of brine and diesel droplets on stainless steel plates and screens (150 mesh) with different surface structures is shown in Figures 4(c) and 4(d). Due to the high corrosion resistance of the stainless steel, the roughness of the pleated structure prepared under the etching system is low, and obtaining the material superhydrophobicity is not sufficient. By introducing a nano-structure on the etched surface, the superhydrophobic capacity of the stainless steel substrate can be achieved. After EPD, the contact angle between the MN-SS surface and brine droplets is as high as 166 ± 2.6°, the diesel is completely diffused and the contact angle is 0°. These phenomena further confirm that the introduction of nanoscale structures into the microstructure of stainless steel can effectively improve the wettability of stainless steel materials. The screen substrate with micro-nano hierarchical structure shows similar wettability to brine and diesel droplets. The contact angle and sliding angle of the brine are 163 ± 2.8° and 4 ± 1.7°, respectively, showing excellent superhydrophobicity.

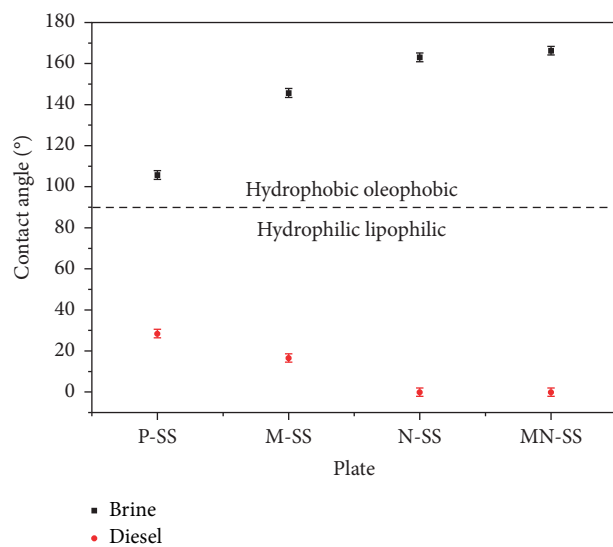
The oil-water separation experiment was also carried out by using the super-hydrophobic/lipophilic stainless steel screens (150 mesh). The superhydrophobic stainless steel screen was rolled into a three-layer cylindrical structure with two ends connected to the input and output pipes with the external diameter of 6 mm, and they were placed



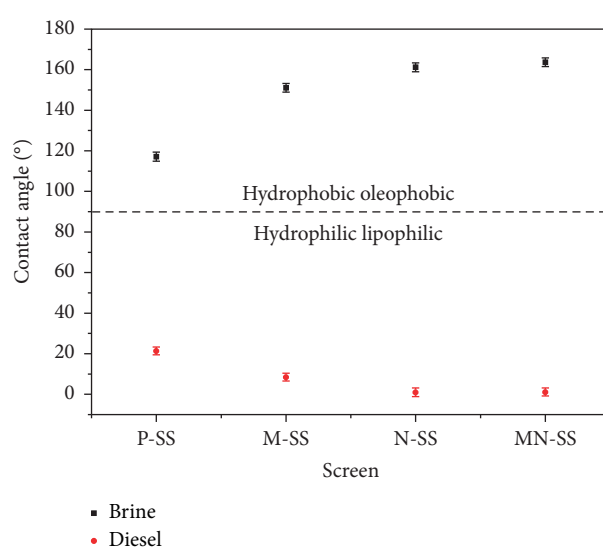
(a)



(b)

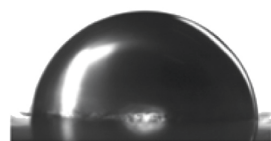


(c)



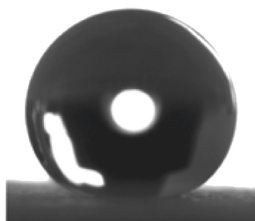
(d)

(e-1)



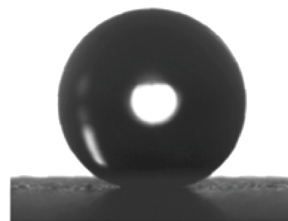
CA = 106 ± 1.5°

(e-2)



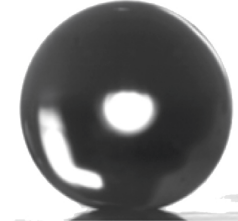
CA = 157 ± 2.8°

(e-3)



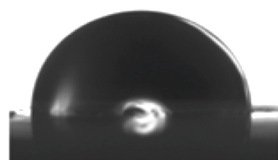
CA = 163 ± 1.2°

(e-4)



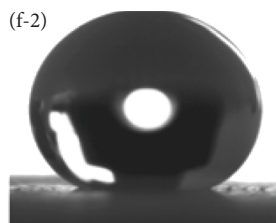
CA = 167 ± 2.1°

(f-1)



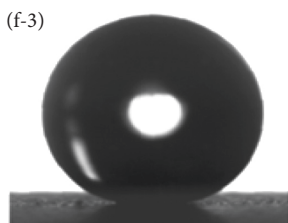
CA = 106 ± 1.4°

(f-2)

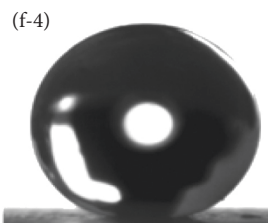


CA = 147 ± 2.1°

(f)



CA = 163 ± 2°



CA = 166 ± 2.6°

FIGURE 4: Continued.



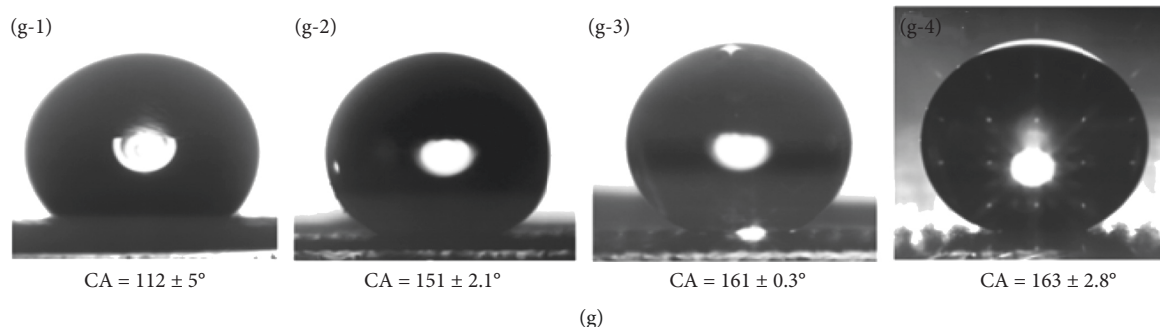


FIGURE 4: The different wettability of brine and diesel on (a, b) Al alloy and (c, d) stainless steel substrates. The contact angle (CA) image of brine on (e) P-Al, M-Al, N-Al, and MN-Al plates and stainless steel (f) plates and (g) screens, all the samples were modified by STA. The magnification scale was 0.5 mm.

horizontally. The length between the ends of the cylindrical structure was referred to as the effective separation length, where the effective separation length was 3 cm. The oil-water mixture with a volume ratio of 1:1 was delivered to the superhydrophobic screen at a rate of  $2 \text{ g} \cdot \text{s}^{-1}$  under the action of a pump. All joints were sealed with adhesive and Teflon tape. This method allows the diesel to be sufficiently contacted with the separation material to avoid the inefficient separation due to the difference in density between the oil and water. During continuous oil-water separation, it could be seen that the brine passed directly through the separation material, while the diesel quickly penetrated the screen and fell into the beaker below.

The purity of the oil collected after separation was tested according to the chemical reaction:



The prepared  $\text{AgNO}_3$  test solution was added to the recovered diesel oil, and it was found that no white flocculated precipitate visible to the naked eye was formed. It was confirmed that there was no NaCl in the mixed solution, thereby demonstrating that there was no brine. Therefore, it can be determined that after the separation of the diesel brine mixture in the separation experiment, the purity of the diesel is extremely high.

**3.3. Analysis of the Influence of Different Modifiers on Surface Wettability.** We studied the effects of different modifiers on the hydrophobicity of nanostructure materials. We used saturated brine ( $\text{NaCl}$ : 17.27 wt.%,  $\text{Na}_2\text{SO}_4$ : 6.43 wt.%) and diesel (No. 0 diesel) droplets to evaluate the different wetting properties of the blank treatment, EPD treatment, EPD-STA treatment, and EPD-FAS treatment stainless steel samples and obtain corresponding wettability data. Experimental results show that the blank stainless steel plate exhibits hydrophilic-lipophilicity due to the higher surface energy, and the contact angles with the brine and diesel droplets are  $56^\circ$  and  $21^\circ$ , respectively. When the sample is tilted by  $90^\circ$ , water or oil droplets adhering to the surface cannot fall off. However, after the introduction of nano-Al film, the wettability of the surface of the sample changed significantly.

Both the brine and the diesel droplets could spread rapidly on the surface, and the contact angles were all  $0^\circ$ , showing a super-hydrophilic/lipophilic property. After the rough surface was in contact with the STA to reduce the surface energy, the wettability of the brine droplets and the diesel droplets changed differently. The contact angle between the sample and the brine increased to  $163 \pm 2^\circ$ , and the sliding angle was reduced to  $3 \pm 1^\circ$ , and the diesel fuel could still spread rapidly with a contact angle close to  $0^\circ$ . This shows that after modification by STA, the super-hydrophilic/lipophilic material is transformed into the super-hydrophobic/lipophilic material. The above results further confirm that the superhydrophobicity of the sample comes from the synergistic effect of the surface roughness and the self-assembled low surface energy stearic acid.

Next, the effect of using FAS instead of STA as the modifier on the wettability of the N-SS was investigated. The contact angle of the brine droplets after FAS modification slightly increased to  $165 \pm 1.2^\circ$ , indicating that the sample was more hydrophobic. Since the  $-\text{CF}_3$  group at the end of the long chain of the FAS molecule has a lower surface free energy than the  $-\text{CH}_3$  at the end of the STA, this difference in terminal groups helped to conclude that the reduction in surface energy will inevitably lead to an increase in contact angle when the surface roughness is the same [40]. However, such an excessively low surface tension of fluorine-containing material is disadvantageous for oil-water separation [41] because the FAS modified sample exhibited a certain degree of oleo-phobic property, and its contact angle between the sample and the diesel increased to  $108 \pm 0.7^\circ$ .

To further study the modification process, the chemical composition of the sample surface after modification using different low surface energy modifiers was analyzed by FTIR. Figure 5(a) shows the FTIR spectra of unmodified surfaces and pure stearic acid modified N-Al and N-SS surfaces. The modified two surfaces exhibit strong hydroxyl stretching vibration absorption peaks at  $3520 \text{ cm}^{-1}$  due to the presence of hydrogen bonds. At the same time, the new absorption peaks near the wavelength of  $2849 \text{ cm}^{-1}$  and  $2917 \text{ cm}^{-1}$ , respectively, represent the antisymmetric stretching vibration peak and the symmetric stretching vibration peak of

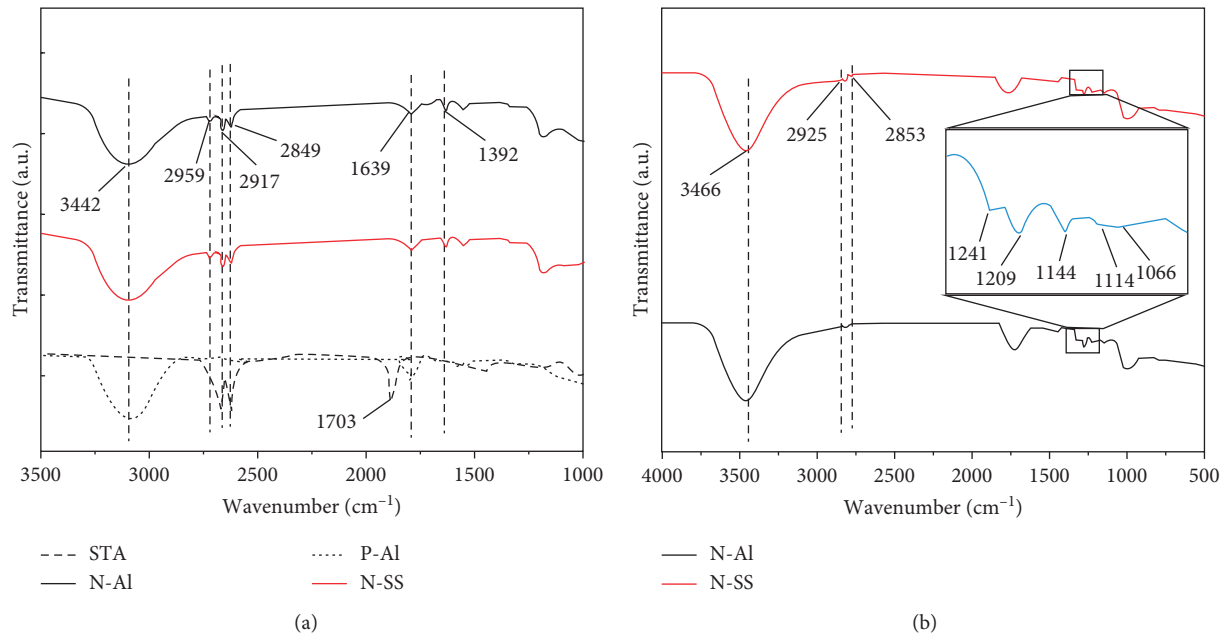


FIGURE 5: FTIR patterns of N-SS and N-Al prepared after EPD and modified by (a) STA and (b) FAS.

-CH<sub>2</sub>-. Besides, the new absorption peak near 2959 cm<sup>-1</sup> is due to the antisymmetric stretching vibration of the -CH<sub>3</sub> group and it has been found that the surface of the sample contains a large number of hydrophobic groups such as -CH<sub>2</sub>- and -CH<sub>3</sub>, which are the key to the formation of a low free energy surface. In addition, Al alloy surface filled with long-chain fatty acids shows two new absorption peaks at 1639 cm<sup>-1</sup> and 1392 cm<sup>-1</sup>, corresponding to the antisymmetric stretching vibration peak and the symmetric stretching vibration peak of -OCO-. Furthermore, the vibration peak at 1703 cm<sup>-1</sup> (corresponding to the typical C=O free stretching vibration peak of stearic acid) disappears unlike what happens with pure stearic acid. We conjectured that the stearic acid molecules dissociate on the surface to form a partially protonated surface with C<sub>12</sub>H<sub>23</sub>O<sub>2</sub>-Al as a structural unit and then self-assemble to form the nano-Al film using a specific method [42]. The molecular structure and self-assembly mechanism of stearic acid are shown in Figure 6(a). According to the results of FTIR characterization, during the modification process, the carboxyl group in STA reacts with the hydroxyl group on the surface of the sample to form a self-assembled film composed of a new compound CH<sub>3</sub>(CH<sub>2</sub>)<sub>16</sub>COO-Al. The analysis revealed that the hydrophilic groups -COO and -OH are bonded to the surface of the Al film, and the hydrophobic groups -CH<sub>3</sub> and -CH<sub>2</sub>- at the end are exposed to the outside and the grafted type of molecular film formed is densely and orderly arranged with superhydrophobicity properties.

The FTIR spectrum after FAS modification is shown in Figure 5(b). On the surface of the two substrates, a strong hydroxyl (-OH) stretching vibration absorption peak appears at 3446 cm<sup>-1</sup>. At the same time, absorption peaks at 2925 cm<sup>-1</sup> and 2853 cm<sup>-1</sup> refer to the antisymmetric stretching vibration and the symmetric stretching vibration of -CH<sub>2</sub>-, respectively. The wavelengths around 1241, 1209, 1144, and 1114 cm<sup>-1</sup> correspond to the stretching vibration peaks of C-F bonds in

-CF<sub>2</sub>- or -CF<sub>3</sub>. In addition, an asymmetric stretching vibration peak of Si-O-Si is detected at 1066 cm<sup>-1</sup>. During the experiment, the N-Al sample is immersed in the FAS ethanol modification solution, which will then trigger the hydroxylation reaction and the dehydration condensation reaction between the FAS molecule and the sample surface [43]. In the first place, the silicon ethoxy group (Si-OCH<sub>2</sub>CH<sub>3</sub>) on the FAS molecule reacts with water to form silicon hydroxyl groups (Si-OH), which can act as reactive at the end of the macromolecule. These silicon hydroxyl groups are further subjected to dehydration and condensation reactions with hydroxyl groups on the surface of the Al, generating polysiloxane-like substances to form a self-assembled low surface energy layer, which is grafted to the surface of the sample in the vertical direction. Meanwhile, condensation reactions occur between adjacent molecules, and finally a continuous, dense, ordered graft type of high polysiloxane is formed on the surface of the Al film, leading to the effective reduction of the surface energy. The reaction mechanism of FAS molecules on the surface of the deposited Al film is shown in Figure 6(b).

**3.4. Effect of Preparation Parameters on Surface Morphology and Wettability Analysis.** Although the etching process is simple, there are still many factors affecting the final morphology during rough surface formation. Due to the high level of influence the etching morphology has on the final micro-nano hierarchical morphology, the etching time and etchant composition were investigated for their effects on sample morphology and wettability to determine the optimum etch process conditions.

Figures 7(a)–7(d) show the FESEM image of the Al alloy sample surface prepared during etching times of 1, 3, and 10 minutes as well as contact angle and sample quality as a function of the etching time. When the Al alloy substrate is

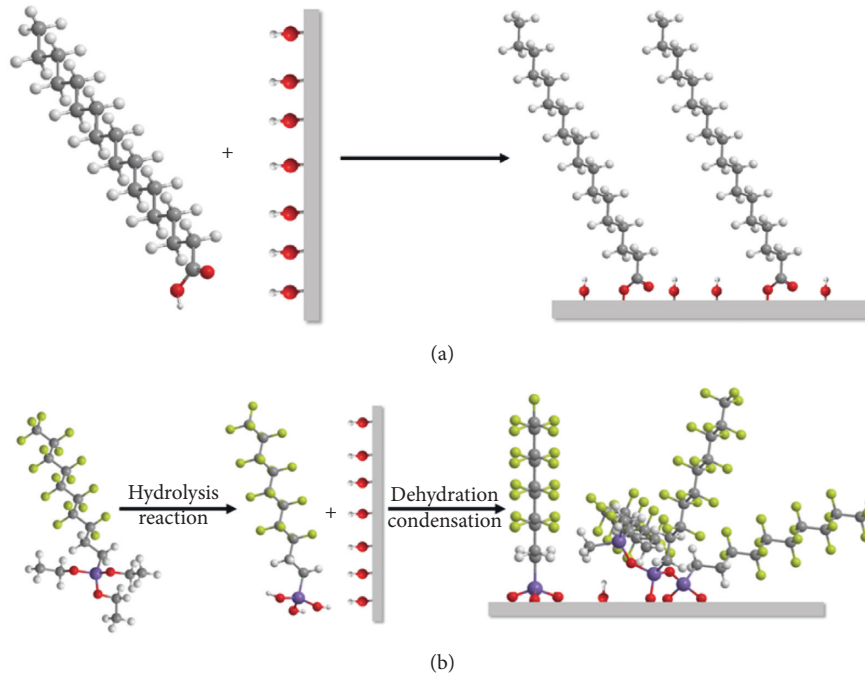


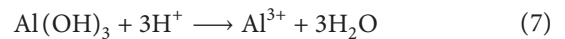
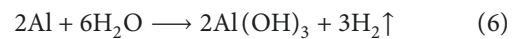
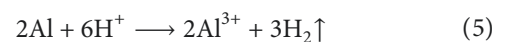
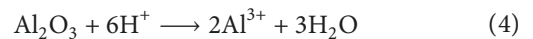
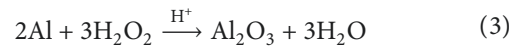
FIGURE 6: Schematic illustration of the formation of self-assembled (a) STA film layer and (b) FAS film layer on the deposited nano-Al film surface.

etched in a mixed solution of 2 mol/L HCl and 2 mol/L  $\text{H}_2\text{O}_2$  for 1 minute, its surface begins to corrode, but still maintains large unetched areas. When the etching time is extended to 3 minutes, the unetched area completely disappears, and a typical Al alloy-layered labyrinth structure with uniformity is formed on the surface. Accordingly, the brine contact angle is  $157^\circ$  and the sliding angle is reduced to about  $6^\circ$ . As the time continues to extend to 10 minutes, it was found that the micron-scale morphology of the sample surface does not appear to change anymore, and the contact angle and sliding angle are  $156 \pm 1.5^\circ$  and  $9 \pm 2.5^\circ$ , respectively. However, the quality of the sample drops sharply during the etching time. Therefore, in the process of etching the micro-morphology of the Al alloy under the HCl/ $\text{H}_2\text{O}_2$  system, an ideal rough micro-morphology can be obtained with an etching time of 3 minutes without causing excessive corrosion to the substrate.

Figure 7(e) shows the contact angle and mass change curves of the stainless steel sample with different etching time. Figures 7(f) and 7(g) show surface FESEM images for 1 minute and 10 minutes etching time. When the etching time is 1 minute, many pleated undulations are distributed on the sample surface, but the height difference of the undulating structure is small. The surface after modification does not reach superhydrophobicity, and the contact angle is  $114 \pm 3^\circ$ . When the etching time is extended to 5 minutes, the sample reaches a higher hydrophobicity. As the time continues to extend to 10 minutes, the surface of the pleated undulating structure has a large height difference, but the contact angle hardly changes. However, the quality of the sample drops sharply. Therefore, a mixed solution of HCl and  $\text{H}_2\text{O}_2$  is selected and etched for 5 minutes to obtain a rough structure required for superhydrophobicity on the surface of the stainless steel.

Below, we will examine the role of the  $\text{H}_2\text{O}_2$  component in the mixed etching solution during the etching process and explore the etching mechanism. Figure 8 shows FESEM photographs of Al alloy surfaces after etching for 3 minutes using mixed solutions of different  $\text{H}_2\text{O}_2$  concentrations (0, 1, and 4 mol/L). As shown, when there is no  $\text{H}_2\text{O}_2$  component in the etching solution, the one-component HCl leaves a vast part of the substrate surface unetched during the etching time. When the  $\text{H}_2\text{O}_2$  concentration is 1 mol/L, the unetched area substantially disappears, and the typical rough structure mentioned above emerges on the surface of the sample, while the number and depth of the etched microscale pits are small. When the concentration is increased to 4 mol/L, the microstructure on the sample surface does not display any significant change.

The dislocation energy present inside the Al alloy is relatively high, and it is preferentially dissolved in HCl [44]. However, we have found that adding  $\text{H}_2\text{O}_2$  to the etching solution accelerates the etching reaction. The mechanism reactions are as follows:



Since  $\text{H}_2\text{O}_2$  exhibits strong oxidizing properties in an acidic environment, the surface of the Al alloy substrate is

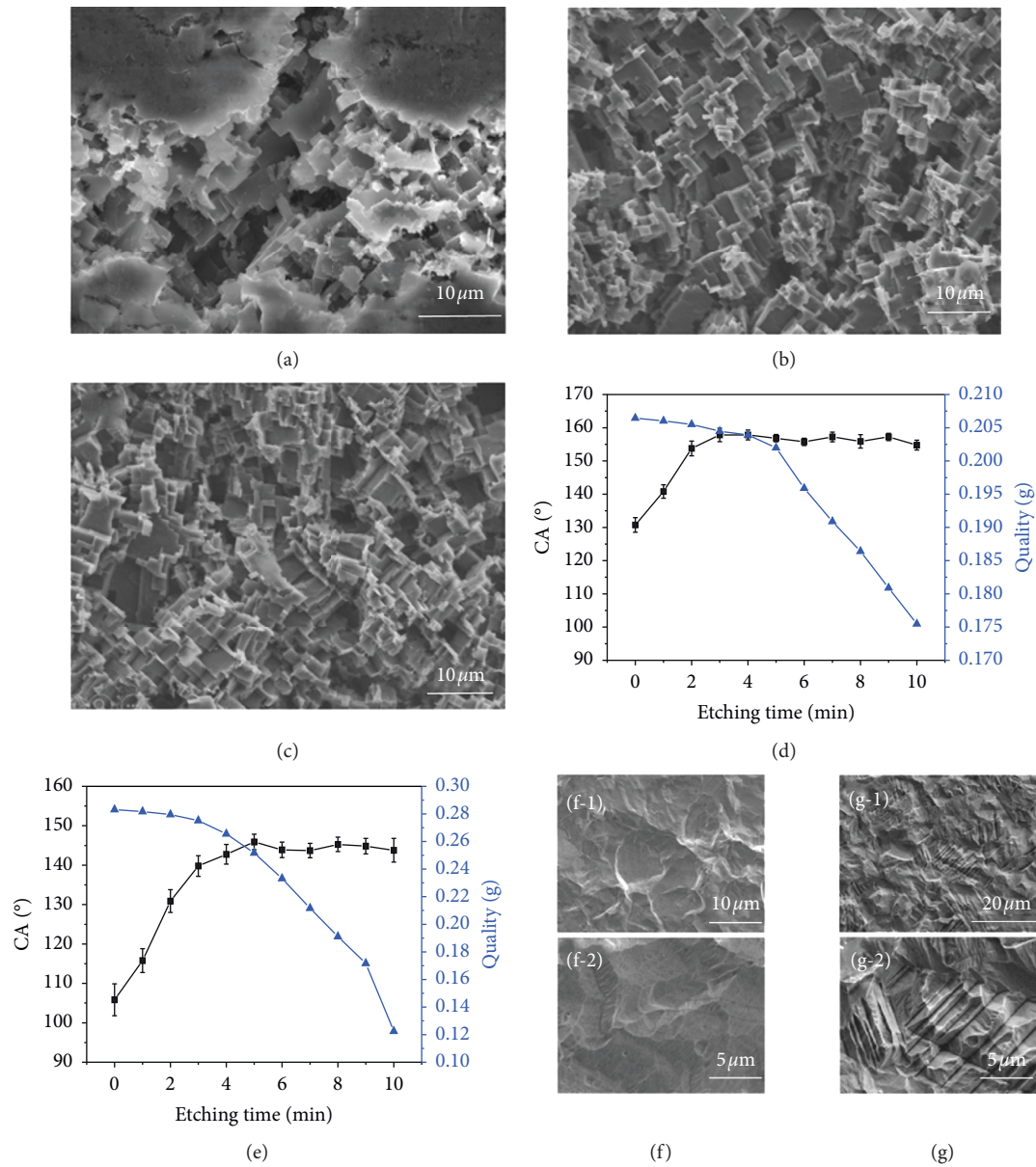


FIGURE 7: FESEM of Al alloy surface after (a) 1 min, (b) 3 min, (c) 10 min etching time and stainless steel surface after (f) 1 min and (g) 10 min etching time. The changes of the brine contact angle and weight of (d) Al alloy sample and (e) stainless steel sample with etching time.

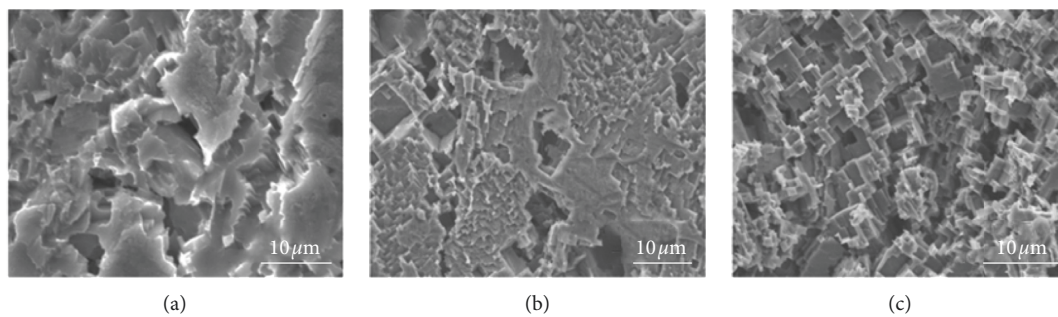
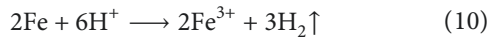
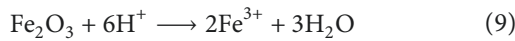
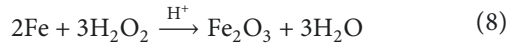


FIGURE 8: FESEM images of the Al alloy surfaces etching with different  $\text{H}_2\text{O}_2$  concentration in 3 min.



rapidly oxidized to  $\text{Al}_2\text{O}_3$ , after the  $\text{H}_2\text{O}_2$  is added to the HCl solution as supported by equation (3). The oxide film is then dissolved by HCl (equation (4)), which is a faster reaction than the one involving HCl and the Al alloy. At the same time, the exposure of the Al alloy substrate to both  $\text{H}^+$  and  $\text{H}_2\text{O}$  leads to reactions (5) and (6), resulting in the etching of the Al alloy surface. Therefore,  $\text{H}_2\text{O}_2$  can accelerate the etching reaction and promote the formation of a rough surface morphology.

For the stainless steel substrate, since  $\text{H}_2\text{O}_2$  exhibits strong oxidizing properties with HCl, the stainless steel surface is rapidly oxidized to  $\text{Fe}_2\text{O}_3$  after the  $\text{H}_2\text{O}_2$  is added to the HCl solution (equation (8)). Since the reaction rate of HCl and  $\text{Fe}_2\text{O}_3$  is faster than that of HCl and Fe, the oxide film is then dissolved by HCl (equation (9)). Substances such as chromium and nickel in the stainless steel substrate will pitting, which together promote the formation of micro-structures. Therefore,  $\text{H}_2\text{O}_2$  can accelerate the etching progress in the reaction. The mechanism reactions are as follows:



The following part of the analysis will discuss the electrophoresis kinetics of nano-Al particles in the system to determine the important parameters for getting the best morphology and wettability. Figure 9(a) describes the deposition quality as a function of the electrophoresis time under constant applied electric fields (5 V/mm, 10 V/mm and 20 V/mm) on the Al alloy substrate. When the applied electric field is fixed, the mass of the deposit increases linearly with time. The fitting relationship between the deposition quality and the deposition time under three electric field strengths is

$$\begin{aligned} y &= 0.22315x; R^2 = 0.9885; x < 5 \text{ min}, \\ y &= 0.46314x; R^2 = 0.9961; x < 5 \text{ min}, \\ y &= 0.80986x; R^2 = 0.9967; x < 5 \text{ min}. \end{aligned} \quad (11)$$

It can be seen that the deposition behavior of nano-Al particles is still linearly controlled in the 5 minutes time interval, which is similar to the electrophoresis dynamic process of the polished blank substrate. It can be seen that the change of the micron-scale roughness of the base material has little effect on the electrophoretic dynamic process of the nano-Al powder. Therefore, the composite morphology prepared by EPD can be effectively controlled by monitoring the time. However, a too long deposition time is not conducive to the formation of micro-nanostructures. Figures 9(b) and 9(c) show the surface topography with an EPD time of 1 minute and 5 minutes, respectively. When the deposition time is 1 minute, there are a large number of exposed micron-scale stepped structures on the surface of the etched Al alloy, and the deposited nanoparticles are only

scattered on the surface of the step structure (Figure 9(b)). As the deposition time increases to 5 minutes, it was found that the micron-scale roughness of the sample surface has been completely covered by the deposited nanoparticles and damaged in a way that the surface structure of the sample was similar to the nano-scale one.

When preparing binary structure film on stainless steel substrates, since the etching morphology is different from that of the Al alloy, and considering the short EPD time, the amount of the deposition material should be strictly controlled. In order to control the amount of electrophoretic deposition, we analyzed the relationship between the EPD quality and EPD time at 10 V/mm. Results showed that in the process of preparing the composite morphology under the suspension system, with a fixed applied electric field, the mass of the deposit increased linearly with time. Therefore, the deposition composite morphology could also be effectively controlled by time monitoring. Figures 9(d) and 9(e) show the contact angle and sliding angle of brine droplets on the surface of the MN-SS as a function of the deposition time. The inset is surface FESEM images of deposition time 1, 3, and 5 minutes. Similar to the Al alloy substrate, the EPD time should not be too long; otherwise, the composite structure will be destroyed.

**3.5. Micro-Nanostructure Surface Durability Analysis.** In order to test the wear resistance of the sample, a simple device was used to quantify the friction resistance of the nano-structure surface and the micro-nano composite structure. The test specimen was attached to the bottom of 500 g mass, which was then placed on the sandpaper with the super-hydrophobic surface facing the sandpaper. The mass was then made to slide on the sandpaper at a certain speed (5 cm/s). The obtained result is shown in Figure 10(a). Afterward, the change in the contact angle and sliding angle of the sample surface after sliding a certain distance was tested.

Figures 10(b)–10(e) show the relationship between the contact angle and the sliding angle of MN-Al, N-Al, MN-SS, and N-SS surfaces as the friction distance increases. On the surface of N-SS, the contact angle of the brine continues to decrease as the friction distance increases and reaches the value  $132 \pm 5^\circ$  after 60 cm. Similarly, after sliding 60 cm, the N-Al surface superhydrophobicity decreases and the contact angle is  $140 \pm 4.5^\circ$ . However, it can be seen from the graph that although the brine contact angles of MN-SS and MN-Al surfaces decrease as the friction distance increases, the rate of decrease is smaller than that of the nanostructure surface. After sliding 60 cm, the surface still shows superhydrophobicity with a contact angle of  $150^\circ$  or more. These phenomena prove that after the microstructure is associated with the deposited nanostructure, the mechanical friction properties of the material are greatly improved.

Figure 11 shows the surface FESEM images of MN-Al (Figures 11(a) and 11(b)) and MN-SS (Figures 11(c) and 11(d)) after sliding 10 cm and 30 cm, respectively. After the initial 10 cm friction, the micro-nano binary structure only causes local damage, and the overall binary structure of the surface of Al alloy and stainless steel are still maintained

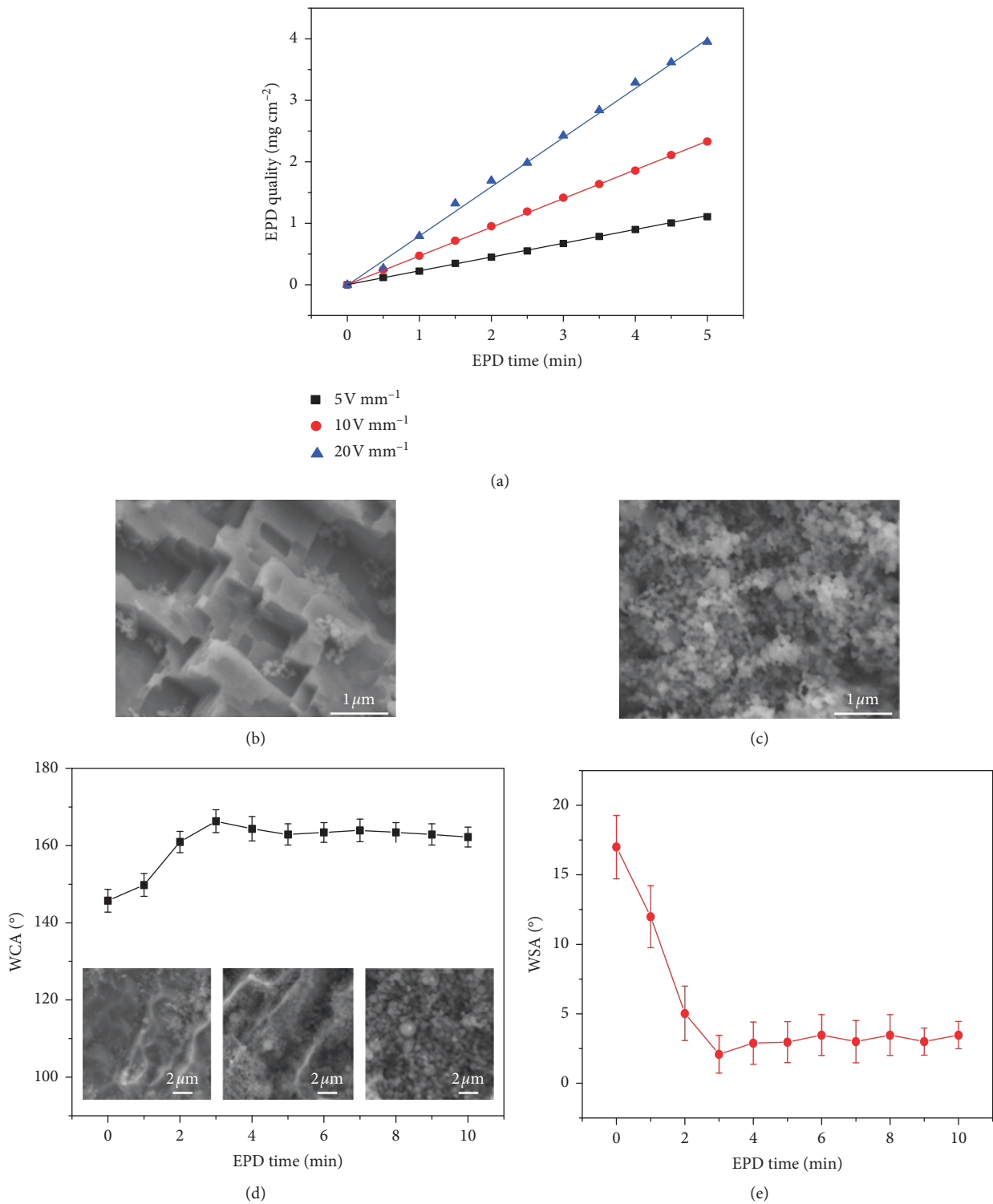


FIGURE 9: (a) The relationship of EPD time and deposited weight per  $\text{cm}^{-2}$  of Al nanoparticles on etched Al alloy, FESEM of surface after (b) 1 min and (c) 5 min EPD time on etched Al alloy surface. Change is the (d) contact angle and (e) sliding angle of the brine on etched stainless steel as a function of the EPD time after STA modification.

(Figures 11(a) and 11(c)). However, after 30 cm of friction, the micro-nanostructure of the entire surface is destroyed (as shown in Figures 11 (b-1) and 11 (d-1)). While from the high-magnification FESEM images (Figures 11 (b-2) and 11 (d-2)),

it can be observed that although the micro-nanostructure found at a higher surface position was destroyed, the one at lower positions was completely preserved due to the protection provided by the higher-strength microstructure. It can

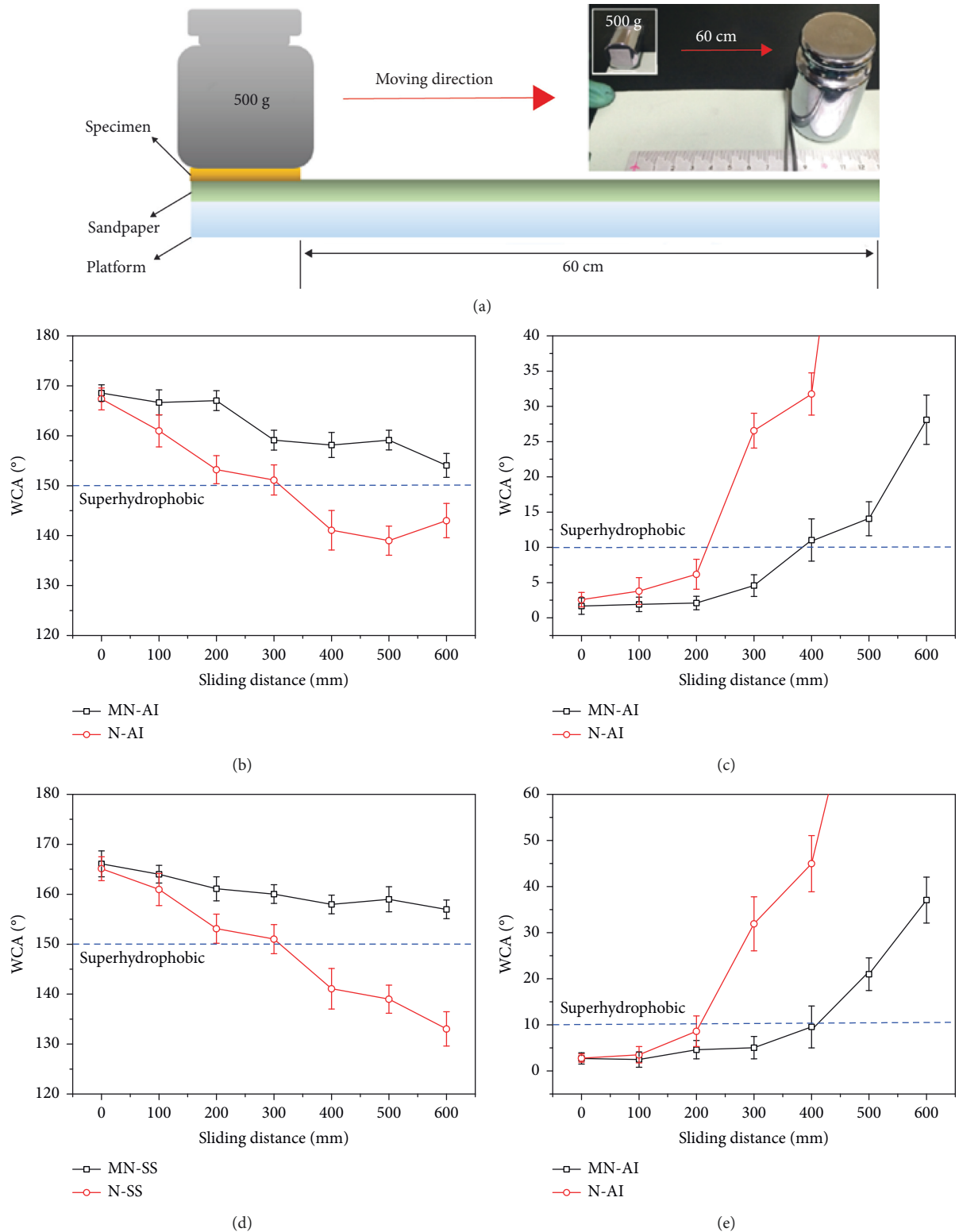


FIGURE 10: (a) Sandpaper abrasion test. (b–e) The contact angle and sliding angle of brine with respect to abrasion length on the MN-Al, N-Al, MN-SS, and N-SS surfaces.

be concluded that the friction of the superhydrophobic surface occurs first in the micro-nano bump structure, which then occurs in the micro-pit area filled by the micro-nano bumps. At the same time, the granular structure caused by

friction was disorderly distributed on the surface, and this favored the development of superhydrophobic properties on the surface. A schematic diagram of its protection mechanism is shown in Figures 11(e) and 11(f).

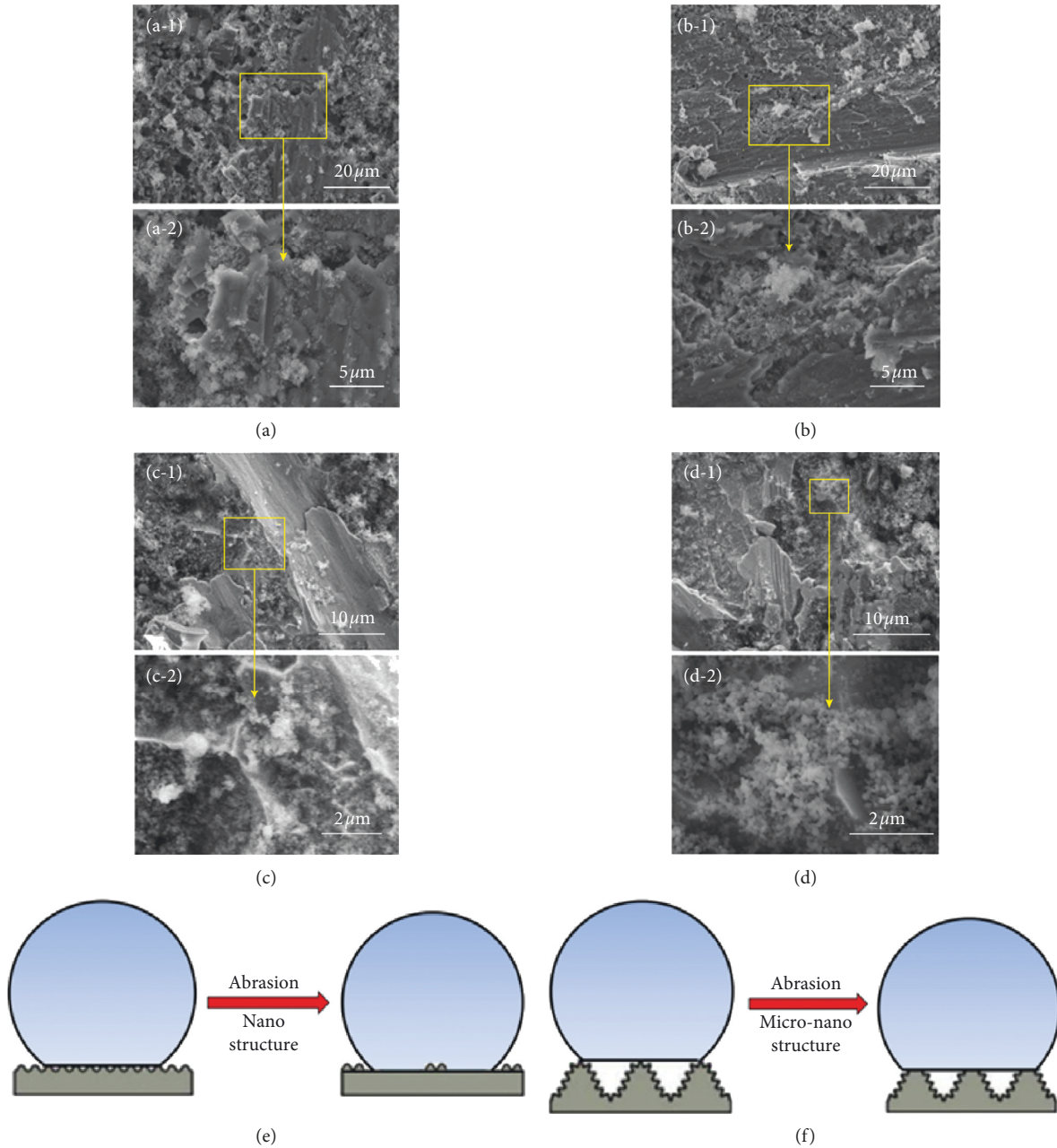


FIGURE 11: (a, b) MN-Al and (c, d) MN-SS surfaces slide at different distances after the low magnification and high-power FESEM images. The resistance abrasion schematic diagram of (e) nanostructured surface and (f) hierarchical structure surface.

For superhydrophobic materials used in the construction of salt rock cavities, the corrosion resistance in a high salt environment directly determines the promotion effect. According to the results of on-site sampling, the main components in the brine are NaCl and  $\text{Na}_2\text{SO}_4$ . In order to test the corrosion resistance of superhydrophobic MN-SS and MN-Al in brine environment, the potentiodynamic polarization curves of P-SS, P-Al, superhydrophobic MN-SS, and MN-Al in 3.5 wt.% NaCl solution and 3.5 wt.%  $\text{Na}_2\text{SO}_4$  solution were measured at a scanning speed of  $10 \text{ mV} \cdot \text{s}^{-1}$  using Chenhua Electrochemical Workstation.

Figures 12(a) and 12(b) show the potentiodynamic polarization curves of P-SS and superhydrophobic MN-SS in 3.5 wt.% NaCl solution (Figure 12(a)) and 3.5 wt.%  $\text{Na}_2\text{SO}_4$  solution (Figure 12(b)). It can be seen from the polarization curves that there is a passivation zone in the anode region, indicating that the corrosion reaction on the surface of the super-hydrophobized stainless steel substrate is suppressed to some extent. When taking into consideration the polarization curves, the relevant electrochemical parameters such as the self-corrosion potential ( $E_{\text{corr}}$ ) and the corrosion current density ( $i_{\text{corr}}$ ) can be calculated using the Tafel



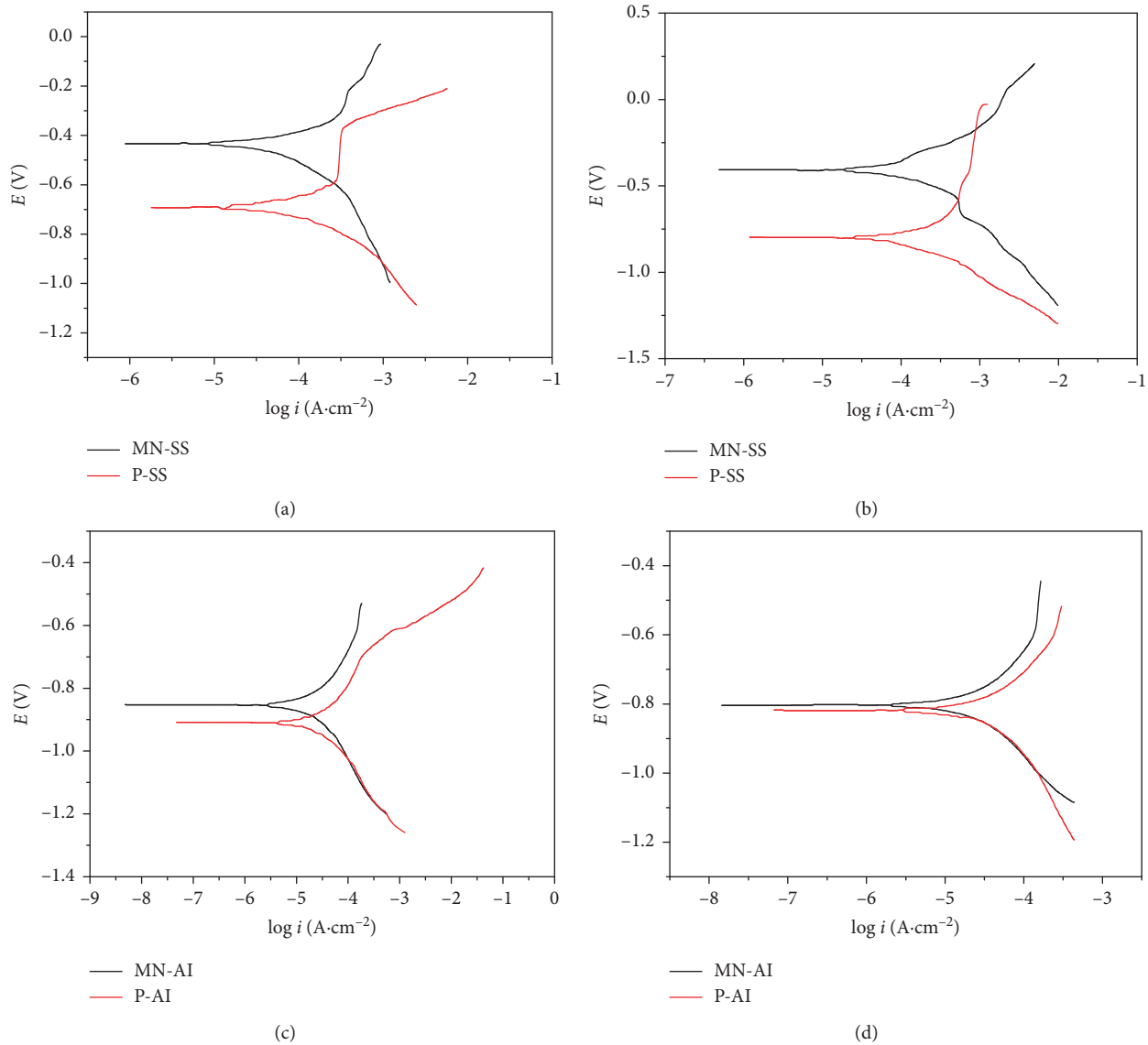


FIGURE 12: Potentiodynamic polarization curves of MN-SS, P-SS in (a) NaCl solution and (b)  $\text{Na}_2\text{SO}_4$  solution and MN-AI, P-AI in (c) NaCl solution and (d)  $\text{Na}_2\text{SO}_4$  solution.

formula [45]. The results are shown in Table 1. The table shows that the self-corrosion potential of the superhydrophobic MN-SS is improved relative to P-SS in 3.5 wt.% NaCl solution and 3.5 wt.%  $\text{Na}_2\text{SO}_4$  solution. At the same time, the corrosion current density of the superhydrophobic MN-SS decreases by one order of magnitude relative to the P-SS. The superhydrophobic MN-SS has a corrected self-corrosion potential and a lower corrosion current density [46], indicating that the prepared superhydrophobic MN-SS can significantly improve the corrosion resistance of P-SS. Figures 12(c) and 12(d) show the potentiodynamic polarization curves of P-AI and the superhydrophobic MN-AI in 3.5 wt.% NaCl solution (Figure 12(c)) and 3.5 wt.%  $\text{Na}_2\text{SO}_4$  solution (Figure 12(d)). With the addition of the polarization curves, the relevant electrochemical parameters can also be calculated. The results are shown in Table 2, which indicate that the prepared superhydrophobic MN-AI can also significantly improve the corrosion resistance of P-AI.

For an oil-containing brine separation material, the surface may have special chemical properties, and the surrounding environment may have an effect on its wettability. We tested the stability of the separation materials under different conditions by air exposure experiments, diesel/brine soaking experiments, and wettability reproducibility experiments. The obtained results are shown in Figure 13.

Figure 13(a) shows the change trend of the brine contact angle and sliding angle of the separation materials after exposition for different time lengths in a room temperature environment. Surprisingly, the superhydrophobicity of the surface has excellent long-term stability. Even after standing in the air for more than 6 months, the contact angle of the brine/diesel droplets of the materials do not change substantially, and the apparent brine contact angle is still above  $153^\circ$ , while the sliding angle remains less than  $10^\circ$ , displaying super-hydrophobic/lipophilic properties.

TABLE 1: The electrochemical parameters of potentiodynamic polarization curves.

Sample	3.5 wt.% NaCl solution		3.5 wt.% Na <sub>2</sub> SO <sub>4</sub> solution	
	Self-corrosion potential $E_{\text{corr}}$ (V)	Corrosion current density $i_{\text{corr}}$ (A/cm <sup>2</sup> )	Self-corrosion potential $E_{\text{corr}}$ (V)	Corrosion current density $i_{\text{corr}}$ (A/cm <sup>2</sup> )
MN-SS	-0.429	$5.978 \times 10^{-5}$	-0.405	$8.180 \times 10^{-5}$
P-SS	-0.688	$1.046 \times 10^{-4}$	-0.795	$1.197 \times 10^{-4}$

TABLE 2: The electrochemical parameters of potentiodynamic polarization curves.

Sample	3.5 wt.% NaCl solution		3.5 wt.% Na <sub>2</sub> SO <sub>4</sub> solution	
	Self-corrosion potential $E_{\text{corr}}$ (V)	Corrosion current density $i_{\text{corr}}$ (A/cm <sup>2</sup> )	Self-corrosion potential $E_{\text{corr}}$ (V)	Corrosion current density $i_{\text{corr}}$ (A/cm <sup>2</sup> )
MN-Al	-0.850	$2.248 \times 10^{-5}$	-0.802	$2.424 \times 10^{-5}$
P-Al	-0.907	$5.005 \times 10^{-5}$	-0.817	$3.248 \times 10^{-5}$

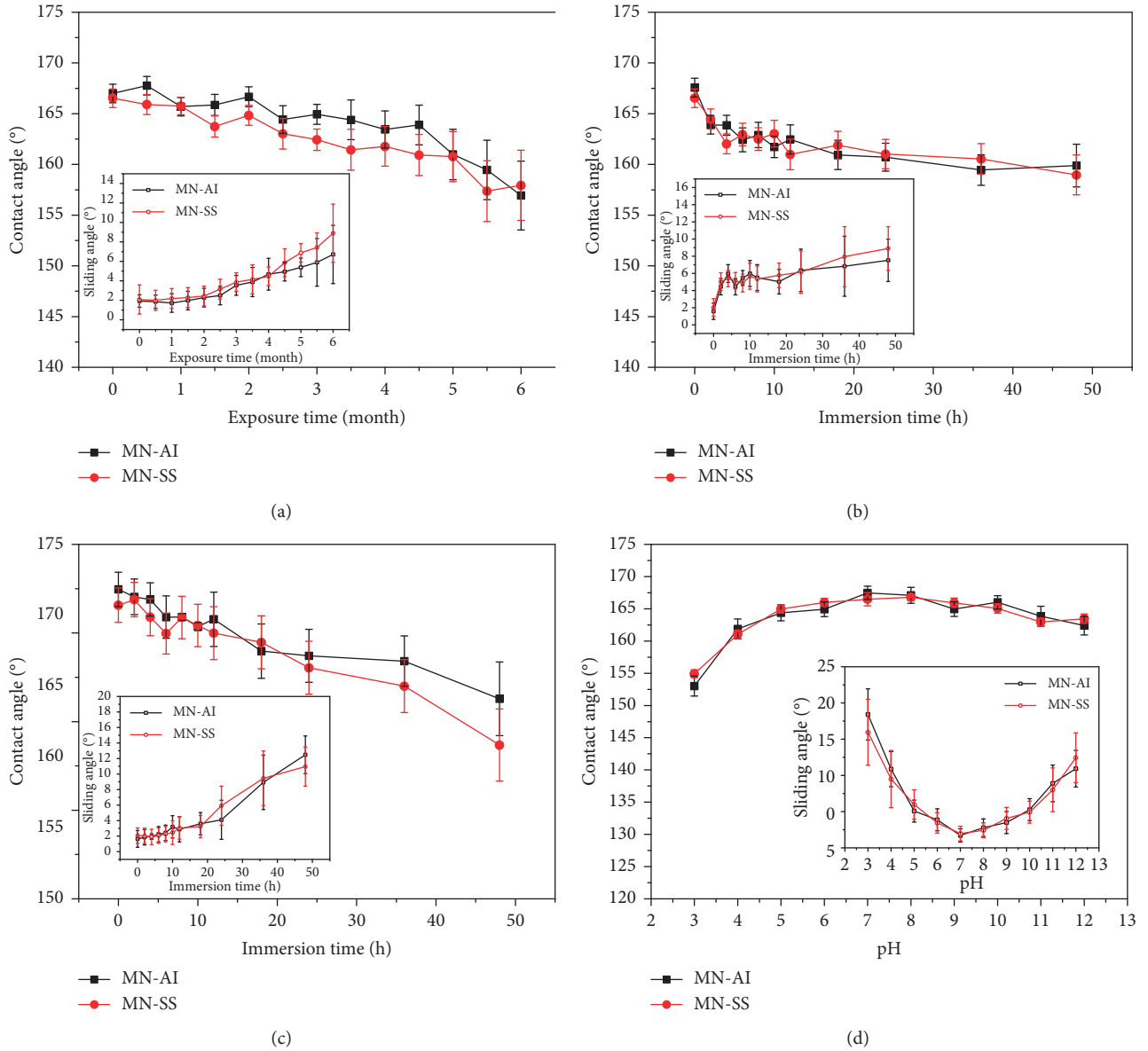


FIGURE 13: The changes of contact angle and sliding angle of MN-SS and MN-Al surface with the (a) exposure time, (b) immersion time in oil, (c) immersion time in brine, and (d) pH value.

Figure 13(b) shows the change trend of the surface wetting reproducibility after the sample is immersed in diesel for 48 h. Samples were taken out of the diesel every hour and thoroughly rinsed with alcohol and tested for changes in the contact angle and the sliding angle. The wetting reproducibility was tested by repeating the soaking and observing the change in contact angle. Results show that the wettability does not change with the immersion time, and the repeated diesel wetting and drying process has no obvious effect on the super-hydrophobic/lipophilic properties of the sample. This also shows that the material can be repeatedly subjected to the oil-water separation process.

Figure 13(c) shows the change in contact angle and sliding angle after immersion in the brine solution for 48 hours. Unlike diesel soaking, the surface of the sample is not wetted after immersion in brine, but the contact angle and sliding angle of the material changed slightly during the soaking for different brine concentrations. After 48 h of soaking, the contact angle of MN-Al and MN-SS dropped to  $158 \pm 4^\circ$  and  $162 \pm 4^\circ$  respectively, and the sliding angle increased. This might be due to the fact that the stearic acid molecules grafted on the surface of the material in contact with the brine are soaked and stripped by the brine, thus damaging the wettability. However, the surface contact angle of MN-SS after soaking for 48 h is still as high as  $160^\circ$ . The results also show that the micro-nano surface material can maintain a stable superhydrophobic property in the brine environment.

Figure 13(d) shows the change in the contact angle and sliding angle of water droplets with different pH. For strong acid droplets, the hydrophobic properties of the MN-Al and MN-SS surfaces are slightly reduced but still maintain a certain superhydrophobicity. This is because although the surface deposits are metallic nanoparticles, they are nevertheless wrapped by long-chain alkanes, which form a hydrophobic protective layer. The observation of the entire sample reveals that the real solid-liquid contact area is small, and therefore, the corrosion rate of the strong acid is slowed down for either the single nanoparticles or the whole sample. Similarly, strong alkali droplets also exhibit superhydrophobicity on the surface of MN-Al and MN-SS. Test results further indicate that the prepared surface exhibits superhydrophobicity property for both acid and alkali droplets.

## 4. Conclusions

- (1) After chemical etching under the HCl/H<sub>2</sub>O<sub>2</sub> system, a large number of micro-sized discontinuous pits and rectangular boss structures are formed on the surface of Al alloy substrates while a large number of micron-sized pit structures and irregularly shaped pleats for the stainless steel substrate surface, leading to different micro-nanostructure finally.
- (2) Both substances exhibit super-hydrophobic/lipophilic properties with STA modification and have a higher level of improvement compared to the single-structured surface of micron or nano. The contact angles of the brine on MN-Al and MN-SS surfaces increase to  $167 \pm 2.1^\circ$  and  $166 \pm 2.6^\circ$ , respectively, and the diesel is completely diffused.

- (3) Samples with a nanostructure are modified by STA and FAS for investigating the influence of different modifiers on surface wettability and learn that FAS modified samples display a certain oleophobic property, disqualifying it to be used as a modifier in this case.
- (4) For Al alloy substrates, an ideal rough micromorphology can be obtained for an etching time of 3 min under the HCl/H<sub>2</sub>O<sub>2</sub> system, while 5 min is needed for the stainless steel substrates. Results show that H<sub>2</sub>O<sub>2</sub> can accelerate the etching reaction due to its strong oxidizing properties in an HCl solution. And electrophoretic deposition quality shows a linear relationship with the electric field strength and electrophoresis time within a specific time duration for both Al alloy and stainless steel substrates.
- (5) The micro-nano hierarchical structure has a better wear resistance, better corrosion resistance, and long-term stability and therefore is well adapted to the corrosive environment of high-concentration brine and the harsh working environment on the site.

## Abbreviations

P-Al:	Polished aluminum
M-Al:	Microstructured aluminum
N-Al:	Nanostructured aluminum
MN-Al:	Micro/nanostructured aluminum
P-SS:	Polished stainless steel
M-SS:	Microstructured stainless steel
N-SS:	Nanostructured stainless steel
MN-SS:	Micro/nanostructured stainless steel
EPD:	Electrophoretic deposition
STA:	Stearic acid
FAS:	1H,1H,2H,2H-Perfluorodecyltriethoxysilane
FESEM:	Field emission scanning electron microscope
FTIR:	Fourier transform infrared spectrophotometer.

## Data Availability

The present article addresses methodological issues and does not use or refer to any specific datasets.

## Conflicts of Interest

The authors declare that they have no conflicts of interest.

## Authors' Contributions

Li Depeng and Ngaha Tiedeu William performed the experiments. Chen Jie and Jiang Deyi analyzed the data. Fan Jinyang wrote the paper and Ngaha Tiedeu William polished the language.

## Acknowledgments

This work was supported by the Natural Science Fund (nos. 51834003 and 51574048), Chongqing Postdoctoral Innovation Program (CQBX201805), and Fundamental Research Funds for the Central Universities (nos. 2018CDQYZH0018 and

cqu2018CDHB1B09), which are all greatly appreciated. The authors would like to thank Zhibo Wei and Zhe Xu for their assistance during experiments.

## References

- [1] J. Fan, J. Chen, D. Jiang, A. Chemenda, J. Chen, and J. Ambre, "Discontinuous cyclic loading tests of salt with acoustic emission monitoring," *International Journal of Fatigue*, vol. 94, pp. 140–144, 2017.
- [2] J. Fan, D. Jiang, W. Liu, F. Wu, J. Chen, and J. Daemen, "Discontinuous fatigue of salt rock with low-stress intervals," *International Journal of Rock Mechanics and Mining Sciences*, vol. 115, pp. 77–86, 2019.
- [3] W. Liu, Z. Zhang, J. Chen et al., "Physical simulation of construction and control of two butted-well horizontal cavern energy storage using large molded rock salt specimens," *Energy*, vol. 185, pp. 682–694, 2019.
- [4] T. Ren, D. Y. Jiang, J. Chen, Q. X. Li, and S. Ren, "The research progress of key technology on building energy underground storage in salt rock," *Advanced Materials Research*, vol. 512–515, pp. 1083–1088, 2012.
- [5] M. Ma, Y. Mao, M. Gupta, K. K. Gleason, and G. C. Rutledge, "Superhydrophobic fabrics produced by electrospinning and chemical vapor deposition," *Macromolecules*, vol. 38, no. 23, pp. 9742–9748, 2005.
- [6] S. Wang, L. Feng, H. Liu et al., "Manipulation of surface wettability between superhydrophobicity and superhydrophilicity on copper films," *Chemphyschem*, vol. 6, no. 8, pp. 1475–1478, 2005.
- [7] Y. Jikang, L. Xiaogang, A. Ozge et al., "Superwetting nanowire membranes for selective absorption," *Nature Nanotechnology*, vol. 3, pp. 332–336, 2008.
- [8] D. Mysore, T. Viraraghavan, and Y. C. Jin, "Oil/water separation technology—a review," *Journal of Residuals Science and Technology*, vol. 3, pp. 5–14, 2006.
- [9] J. C. Yi, F. C. Mei, C. L. Law, and D. G. Hassell, "A review on anaerobic–aerobic treatment of industrial and municipal wastewater," *Chemical Engineering Journal*, vol. 155, pp. 1–18, 2009.
- [10] S. Vemu and U. B. Pinnamaneni, "Cross-flow microfiltration of industrial oily wastewater: experimental and theoretical consideration," *Separation Science and Technology*, vol. 46, pp. 1213–1223, 2011.
- [11] S. A. Sayed and A. M. Zayed, "Investigation of the effectiveness of some adsorbent materials in oil spill clean-ups," *Desalination*, vol. 194, no. 1–3, pp. 90–100, 2006.
- [12] V. Janout, S. B. Myers, R. A. Register, and S. L. Regen, "Self-cleaning resins," *Journal of the American Chemical Society*, vol. 129, no. 17, pp. 5756–5759, 2007.
- [13] T.-T. Lim and X. Huang, "In situ oil/water separation using hydrophobic-oleophilic fibrous wall: a lab-scale feasibility study for groundwater cleanup," *Journal of Hazardous Materials*, vol. 137, no. 2, pp. 820–826, 2006.
- [14] B. Hu and K. Scott, "Influence of membrane material and corrugation and process conditions on emulsion microfiltration," *Journal of Membrane Science*, vol. 294, no. 1–2, pp. 30–39, 2007.
- [15] H. Y. Yildirim Erbil, A. Levent Demirel, Y. Avci, and O. Mert, "Transformation of a simple plastic into a superhydrophobic surface," *Science*, vol. 299, no. 5611, pp. 1377–1380, 2003.
- [16] Z. Chu, Y. Feng, and S. Seeger, "Oil/water separation with selective superant wetting/superwetting surface materials," *Angewandte Chemie International Edition*, vol. 54, no. 8, pp. 2328–2338, 2015.
- [17] Z. Xue, Y. Cao, N. Liu, L. Feng, and L. Jiang, "Special wettable materials for oil/water separation," *Journal of Materials Chemistry A*, vol. 2, no. 8, pp. 2445–2460, 2014.
- [18] Y. I. Tarasevich, Z. M. Shkavro, O. O. Shevchuk, and Y. L. Zub, "Adsorption properties of modified filtration materials in water treatment," in *NATO Security through Science Series*, Springer, Dordrecht, Netherlands, 2006.
- [19] S. S. Shen, K. P. Liu, J. J. Yang, Y. Li, R. B. Bai, and X. J. Zhou, "Application of a triblock copolymer additive modified polyvinylidene fluoride membrane for effective oil/water separation," *Royal Society Open Science*, vol. 5, 2018.
- [20] M. Khosravi and S. Azizian, "Preparation of superhydrophobic and superoleophilic nanostructured layer on steel mesh for oil-water separation," *Separation and Purification Technology*, vol. 172, pp. 366–373, 2017.
- [21] L. Kesong and J. Lei, "Metallic surfaces with special wettability," *Nanoscale*, vol. 3, no. 3, pp. 825–838, 2011.
- [22] W. C. Xu, J. Z. Shi, D. L. Li, G. R. Cao, M. K. Feng, and K. T. Wang, "Application of surface modification in hydrophobic and oleophobic materials research," *Materials Research Innovations*, vol. 19, no. 10, pp. S10–S207, 2015.
- [23] T. Hang, H. J. Chen, S. Xiao et al., "TiO<sub>2</sub> nanowire-templated hierarchical nanowire network as water-repelling coating," *Royal Society Open Science*, vol. 4, 2017.
- [24] H. Ying, D. K. Sarkar, and X. G. Chen, "Superhydrophobic nanostructured ZnO thin films on aluminum alloy substrates by electrophoretic deposition process," *Applied Surface Science*, vol. 327, pp. 327–334, 2015.
- [25] L. Yan, B. Yuan, J. Jin, L. Tian, Z. Han, and L. Ren, "Facile fabrication of biomimetic superhydrophobic surface with anti-frosting on stainless steel substrate," *Applied Surface Science*, vol. 355, pp. 1238–1244, 2015.
- [26] H. Bai, L. Zhang, and D. Gu, "Micrometer-sized spherulites as building blocks for lotus leaf-like superhydrophobic coatings," *Applied Surface Science*, vol. 459, pp. 54–62, 2018.
- [27] Y. Zheng, X. Gao, and L. Jiang, "Directional adhesion of superhydrophobic butterfly wings," *Soft Matter*, vol. 3, no. 2, pp. 178–182, 2007.
- [28] Y. Song, Y. Liu, H. Jiang et al., "Mosquito eyes inspired surfaces with robust antireflectivity and superhydrophobicity," *Surface and Coatings Technology*, vol. 316, pp. 85–92, 2017.
- [29] A. Ganne, V. O. Lebed, and A. I. Gavrillov, "Combined wet chemical etching and anodic oxidation for obtaining the superhydrophobic meshes with anti-icing performance," *Colloids and Surfaces A: Physicochemical and Engineering Aspects*, vol. 499, pp. 150–155, 2016.
- [30] N. Valipour Motlagh, R. Khani, and S. Rahnama, "Super dewetting surfaces: focusing on their design and fabrication methods," *Colloids and Surfaces A: Physicochemical and Engineering Aspects*, vol. 484, pp. 528–546, 2015.
- [31] K. Fei, T.-s. Song, H. Wang, D. Zhang, R. Tao, and J. Xie, "Electrophoretic deposition of carbon nanotube on reticulated vitreous carbon for hexavalent chromium removal in a biocathode microbial fuel cell," *Royal Society Open Science*, vol. 4, 2017.
- [32] X. Jin and B. Kasal, "Adhesion force mapping on wood by atomic force microscopy: influence of surface roughness and tip geometry," *Royal Society Open Science*, vol. 3, 2016.
- [33] M. Miwa, A. Nakajima, A. Fujishima, K. Hashimoto, and T. Watanabe, "Effects of the surface roughness on sliding



- angles of water droplets on superhydrophobic surfaces,” *Langmuir*, vol. 16, no. 13, pp. 5754–5760, 2000.
- [34] Z. Wei, D. Jiang, J. Chen, S. Ren, and L. Li, “Fabrication of mechanically robust superhydrophobic aluminum surface by acid etching and stearic acid modification,” *Journal of Adhesion Science and Technology*, vol. 31, no. 21, pp. 2380–2397, 2017.
- [35] A. Marmur, “Wetting on hydrophobic rough surfaces: to be heterogeneous or not to be?,” *Langmuir*, vol. 19, no. 20, pp. 8343–8348, 2003.
- [36] E. H. Yildirim and C. C. Elif, “Range of applicability of the Wenzel and Cassie-Baxter equations for superhydrophobic surfaces,” *Langmuir*, vol. 25, pp. 14135–14145, 2009.
- [37] V. Belaud, S. Valette, G. Stremsdoerfer, M. Bigerelle, and S. Benayoun, “Wettability versus roughness: multi-scales approach,” *Tribology International*, vol. 82, pp. 343–349, 2015.
- [38] Z. Xu, D. Jiang, Z. Wei, J. Chen, and J. Jing, “Fabrication of superhydrophobic nano-aluminum films on stainless steel meshes by electrophoretic deposition for oil-water separation,” *Applied Surface Science*, vol. 427, pp. 253–261, 2018.
- [39] U. Cengiz, M. Z. Avci, H. Y. Erbil, and A. S. Sarac, “Superhydrophobic terpolymer nanofibers containing perfluoroethyl alkyl methacrylate by electrospinning,” *Applied Surface Science*, vol. 258, no. 15, pp. 5815–5821, 2012.
- [40] G. McHale and M. I. Newton, “Frenkel’s method and the dynamic wetting of heterogeneous planar surfaces,” *Colloids and Surfaces A: Physicochemical and Engineering Aspects*, vol. 206, no. 1–3, pp. 193–201, 2002.
- [41] Z. S. Saifaldeen, K. R. Khedir, M. T. Camci, A. Ucar, S. Suzer, and T. Karabacak, “The effect of polar end of long-chain fluorocarbon oligomers in promoting the superamphiphobic property over multi-scale rough Al alloy surfaces,” *Applied Surface Science*, vol. 379, pp. 55–65, 2016.
- [42] Z. Xu, D. Jiang, F. Wu, X. Guo, Z. Wei, and J. Chen, “Preparation and droplet impact dynamics of superhydrophobic nano-aluminum films on metal substrates,” *Journal of Materials Science*, vol. 53, no. 7, pp. 5364–5379, 2018.
- [43] X. Guo, X. Li, Z. Wei, X. Li, and L. Niu, “Rapid fabrication and characterization of superhydrophobic tri-dimensional Ni/Al coatings,” *Applied Surface Science*, vol. 387, pp. 8–15, 2016.
- [44] D. K. Sarkar, M. Farzaneh, and R. W. Paynter, “Superhydrophobic properties of ultrathin rf-sputtered Teflon films coated etched aluminum surfaces,” *Materials Letters*, vol. 62, no. 8–9, pp. 1226–1229, 2008.
- [45] Y.-H. Fang and Z.-P. Liu, “First principles Tafel kinetics of methanol oxidation on Pt(111),” *Surface Science*, vol. 631, pp. 42–47, 2015.
- [46] F. Cao, G.-L. Song, and A. Atrens, “Corrosion and passivation of magnesium alloys,” *Corrosion Science*, vol. 111, pp. 835–845, 2016.

